Annu. Rev. Astron. Astrophys. 1998. 36:131–88

RADIO EMISSION FROM SOLAR FLARES

T. S. Bastian
National Radio Astronomy Observatory,[1] Socorro, New Mexico 87801;
e-mail: tbastian@nrao.edu

A. O. Benz
Institute of Astronomy, ETH-Zentrum, CH-8092 Zürich, Switzerland;
e-mail: benz@astro.phys.ethz.ch

D. E. Gary
Physics Department, New Jersey Institute of Technology, Newark, New Jersey 07102;
e-mail: dgary@njit.edu

KEY WORDS: radio radiation, X rays, γ rays, energy release, particle acceleration

ABSTRACT

Radio emission from solar flares offers a number of unique diagnostic tools to address long-standing questions about energy release, plasma heating, particle acceleration, and particle transport in magnetized plasmas. At millimeter and centimeter wavelengths, incoherent gyrosynchrotron emission from electrons with energies of tens of kilo electron volts to several mega electron volts plays a dominant role. These electrons carry a significant fraction of the energy released during the impulsive phase of flares. At decimeter and meter wavelengths, coherent plasma radiation can play a dominant role. Particularly important are type III and type III–like radio bursts, which are due to upward- and downward-directed beams of nonthermal electrons, presumed to originate in the energy release site. With the launch of *Yohkoh* and the *Compton Gamma-Ray Observatory*, the relationship between radio emission and energetic photon emissions has been clarified. In this review, recent progress on our understanding of radio emission from impulsive flares and its relation to X-ray emission is discussed, as well as energy release in flare-like phenomena (microflares, nanoflares) and their bearing on coronal heating.

[1]The National Radio Astronomy Observatory is a facility of the National Science Foundation, operated under cooperative agreement by Associated Universities, Inc.

0066-4146/98/0915-0131$08.00

1. INTRODUCTION

1.1 *Overview*

Radio observations have played an important part in shaping our understanding of flare physics for 50 years. In the 1960s, radio observations played a central role in establishing the long-standing view that particle acceleration in flares is fundamentally a two-phase process. Early observations of meter wavelength (m-λ) radio bursts of type II, III, and IV led to the conclusion (e.g. Wild et al 1963) that essentially all flares have a first phase of particle acceleration wherein electrons are promptly accelerated to energies of ∼100 keV. The first phase is accompanied by hard X-ray (HXR) emission, microwave (centimeter wavelengths or cm-λ) emission, and m-λ type III bursts. For large flares, a second phase occurs ∼10 min after the first. Here, a shock wave produced by the initial energy release propagates out into the corona and Fermi-accelerates electrons and ions to energies as high as 100 MeV and 1 GeV, respectively. Second-phase acceleration is accompanied by m-λ type II and type IV radio bursts and was thought to be ultimately responsible for geomagnetic effects.

Two developments have led to modifications of the "two-phase" picture. First, a new solar energetic phenomenon was discovered in the early 1970s: coronal mass ejections (CMEs) (Tousey 1973, Gosling et al 1974). Over the past decade, CMEs, not flares, have come to be recognized as the primary drivers of interplanetary and geomagnetic disturbances (Gosling et al 1991, Gosling 1993). On the one hand, it is fair to say that in many respects CMEs have assumed the role of the second-phase accelerator to the extent that they accelerate electrons and ions to high energies, are associated with type II/IV radio bursts, and may produce interplanetary type II bursts (Cane 1984). On the other hand, coronal type II bursts—conventionally classified as a second-phase phenomenon—may have nothing to do with CMEs but instead may be the result of a blast wave initiated in the first phase by an associated flare (Wagner & MacQueen 1983, Gopalswamy & Kundu 1995). Second, with the launch of the *Solar Maximum Mission* (SMM) and the *Hinotori* mission in the early 1980s, it became clear that electrons and ions are accelerated to relativistic energies within seconds in some flares, rather than minutes later (Forrest & Chupp 1983, Yoshimori 1989). Hence, Wild et al's (1963) original proposal, that flares and geomagnetic effects could be understood in terms of a two-phase process driven solely by flares, has given way to a more complex and evolving view that interplanetary disturbances and geomagnetic effects can be understood in terms of two types of solar energetic phenomena—flares and CMEs—whose relationship and causes remain poorly understood (Kahler 1992).

1.2 *Scope of the Review*

Radio emission from flares has been addressed in these volumes previously: in the classic review by Wild et al (1963), in reviews by Marsh & Hurford (1982) and Dulk (1985), and to some extent by Kahler (1992), Haisch et al (1991), and Hudson & Ryan (1995). In this review, we again take up the subject of radio emission from flares, taking the view that flares and CMEs are distinct, albeit related, phenomena. Unlike CMEs, which involve the destabilization and expulsion of a significant portion of the corona, and for which the bulk of the energy is ultimately mechanical in form, flares result from a local release of energy in the Sun's low corona, with the bulk of the energy released going into prompt particle acceleration and plasma heating. Although more refined flare classification schemes have been proposed (Tanaka 1987, Bai & Sturrock 1989, Cliver 1996), the simple designations of "impulsive" flares and "long-duration events" (LDEs) is sufficient here, of which the latter is commonly associated with CMEs. The bulk of this review is directed toward radio emission from impulsive flares. Impulsive flares, which account for the vast majority, place some of the greatest demands on our understanding of energy release and particle acceleration. A large flare may require the acceleration of $\approx 10^{37}$ electrons s^{-1} to energies >20 keV for periods of tens of seconds (e.g. Miller et al 1997). At the opposite extreme, it is now clear that tiny flare-like releases of energy also occur on the Sun more or less continuously, which may have important implications for coronal heating.

Radio emission from flares is rich in diagnostic potential. This is because, unlike HXR emission, for example, a number of distinct emission mechanisms produce radiation at radio wavelengths, both incoherent and coherent mechanisms, from both thermal and nonthermal electron distributions. What questions can radio observations address? We list a few:

When and where is the bulk of the energy released in flares? By what means?

What are the physical properties of the energy release site?

What are the properties of the heated plasma? Of the accelerated particles?

How are heated plasma and accelerated particles transported? To where?

What bearing do flares have on the question of coronal heating?

With these questions in mind, we consider radio emission from impulsive solar flares and flare-like phenomena. In doing so, we compare radio emission from flares with recent observations of energetic photonemissions (X-rays and

γ-rays) that probe populations of energetic particles of direct relevance to radio emission. We do not discuss radio emission from LDEs in any detail, radio bursts conventionally associated with LDEs (type II and type IV bursts), or interplanetary radio bursts.

2. EMISSION AND PROPAGATION OF RADIO WAVES

At radio frequencies, $h\nu \ll k_B T$ (the Rayleigh-Jeans regime). The specific intensity $\mathcal{I}_\nu$ and the source function $\mathcal{S}_\nu$ of the radiation are therefore conveniently expressed in terms of the brightness temperature T_B and the effective temperature $T_{\rm eff}$, where, in a given polarization, $\mathcal{I}_\nu = k_B T_B \nu^2/c^2$ and $\mathcal{S}_\nu = k_B T_{\rm eff} \nu^2/c^2$. For spatially unresolved solar observations, the flux density S_ν is typically expressed in solar flux units (sfu).[2] For imaging instruments, observations are limited in angular resolution to some solid angle, Ω_{bm}, referred to as the "beam." Instead of measuring the specific intensity, the measured quantity is the flux density per beam, where $\langle S_\nu \rangle_{bm} = k_B \langle T_B \rangle_{bm} \nu^2 \Omega_{bm}/c^2$, and $\langle T_B \rangle_{bm}$ is the mean brightness temperature over the beam Ω_{bm}. For an optically thick source and incoherent emission, $T_B = T_{\rm eff}$, where $T_{\rm eff}$ is the kinetic temperature if the emitting source is in thermal equilibrium, and $T_{\rm eff}$ is the mean energy of the emitting electrons otherwise. For an optically thin source, $T_B \approx \tau_\nu T_{\rm eff}$, where τ_ν is the optical depth. Here, the microphysics of the specific emission mechanism is embodied in the absorption coefficient κ_ν through $\tau_\nu = \int \kappa_\nu \, dl$. For coherent emission, one can have $T_B \gg T_{\rm eff}$.

2.1 *Relevant Emission Mechanisms*

In the wavelength range that concerns us here—mm-λ to m-λ—radio emission from the Sun is produced incoherently by continuum processes or coherently by nonlinear resonant processes involving the electron plasma frequency, the electron gyrofrequency, or the harmonics thereof. No spectral lines in emission or absorption resulting from atomic or molecular transitions have been observed in this wavelength range on the Sun. While there has been speculation that radio recombination lines of certain ions may play a role at wavelengths of a few millimeters to several centimeters, several searches in the relevant wavelength bands have yielded no detections. Pressure broadening is so extreme as to render such lines undetectable (see Bastian 1995a and references therein).

The dominant radio emission mechanism during impulsive flares depends on the wavelength observed and local conditions in the flaring source. Thermal free-free emission and absorption is, of course, ubiquitous. Most often, however, incoherent gyrosynchrotron emission dominates the emission at cm-λ and

[2] 1 sfu $= 10^{-19}$ ergs cm^{-2} sec^{-1} Hz^{-1} $= 10^4$ Jansky, where the Jansky is the unit of flux density conventionally employed for observations of sidereal sources.

mm-λ and coherent plasma radiation often dominates at m-λ and dm-λ (decimeter wavelength), although other mechanisms can, and do, occur. We first discuss each of these mechanisms and then touch on additional mechanisms.

GYROSYNCHROTRON RADIATION Electrons moving in a magnetic field experience the Lorentz force and therefore gyrate at the electron gyrofrequency $\nu_{Be}/\gamma = eB/2\pi\gamma m_e c \approx 2.8B/\gamma$ MHz, with B in Gauss. At nonrelativistic energies, electrons emit at low harmonics of ν_{Be} (gyroresonance emission). At mildly relativistic energies—Lorentz factors $1 \lesssim \gamma \lesssim 5$, energies of tens of kilo electron volts to a few mega electron volts—the radiation pattern emitted by the electrons is increasingly beamed and they emit at higher harmonics of the electron gyrofrequency, typically tens to hundreds of times ν_{Be}/γ. Expressions for the gyrosynchrotron emission and absorption coefficients, j_ν^{gs} and κ_ν^{gs}, are somewhat cumbersome because they involve integrations over the electron distribution function in both energy and pitch angle and a summation of Bessel functions and their derivatives over a range of harmonics (Ramaty 1969, Trulsen & Fejer 1970). With modern computing resources, it is now straightforward to evaluate j_ν^{gs} and κ_ν^{gs} using the exact formalism, although approximate expressions are also used (e.g. those of Petrosian 1981, Dulk & Marsh 1982, and Klein 1987).

Gyrosynchrotron emission offers a powerful and sensitive diagnostic of physical conditions in flaring sources. Similar to X-ray radiation, it may be used to infer the electron distribution function and its evolution in time. Unlike X-ray radiation, gyrosynchrotron emission is also a sensitive function of magnetic field strength and orientation and can therefore be used to constrain the coronal magnetic field in the flaring source. The spectrum of gyrosynchrotron emission emitted during a flare typically peaks between 5–10 GHz (see Section 3.4) so that both optically thick and optically thin gyrosynchrotron emissions are accessible for study. In addition to diagnosing properties of the energetic electron distribution and the magnetic field, evidence of Razin suppression at low frequencies may be used to place constraints on the ambient thermal plasma density. Further details are discussed in Section 3.2.

PLASMA RADIATION Plasma radiation is a coherent mechanism involving the nonlinear conversion of electron energy to plasma waves. Plasma waves are then converted to electromagnetic waves with a frequency near ν_{pe} or its harmonic, $2\nu_{pe}$, where $\nu_{pe} = (n_e e^2/\pi m_e)^{1/2} \approx 9000\, n_e^{1/2}$ Hz is the electron plasma frequency and n_e is the electron number density. It is usually operative at dm-λ and m-λ. An example of a phenomenon that produces plasma radiation is a beam of nonthermal electrons, which is unstable to the production of plasma waves that give rise to radio emission: a type III burst (see Section 4.2). An

alternative source of plasma radiation is a loss-cone distribution of electrons, which can excite upper hybrid waves and Bernstein modes (Kuijpers 1974; Section 4.3).

Plasma radiation is an important diagnostic of the electron number density in and near the flaring source. Since it is a coherent mechanism, the intensity of plasma radiation is not easily related to the energy of the electrons driving the emission. However, as the emission occurs at ν_{pe} or its harmonic, mechanisms that produce plasma waves offer a means of tracing the density structure of the corona and gradients therein. It may also provide a means of constraining the magnetic field in the corona (e.g. Suzuki & Dulk 1985). At greater distances from the Sun, the radio emission from interplanetary type III bursts is a favored means of deducing the density profile of the interplanetary medium (IPM) (Dulk 1990).

OTHER EMISSION MECHANISMS Several other radio emission mechanisms may play a role during flares. Interest in the cyclotron maser mechanism has been intense (Holman et al 1980, Melrose & Dulk 1982, Sharma et al 1982, Sharma & Vlahos 1984, Winglee et al 1988, Fleishman 1994, Fleishman & Yastrebov 1994, Willes & Robinson 1996). The cyclotron maser offers a direct and efficient means of accounting for the extreme properties of narrowband spike bursts (Section 4.3) and of transporting energy across magnetic field lines via radio-frequency heating (Melrose & Dulk 1984). Fleishman & Kahler (1992) have suggested that transition radiation may play a role between 500 MHz and 10 GHz. Tajima et al (1990) and Güdel & Wentzel (1993) have considered radiation from electrons accelerated in strong DC electric fields. While these mechanisms are of considerable interest in their own right, their importance to flares has not yet been firmly established by the observations.

2.2 *Propagation of Radio Waves in the Solar Corona*

For most purposes, the coronal medium can be treated as a cold magnetized plasma, and the magnetoionic theory (Ratcliffe 1959, Melrose 1980) is sufficient to describe the propagating electromagnetic modes. These are the extraordinary mode (x-mode), ordinary mode (o-mode), z-mode, and whistler mode. The x- and o-modes are of observational interest because they can propagate from the source to infinity. The z- and whistler modes are prevented from doing so by stopbands in the refractive index. For many applications the propagation of the x- and o-modes is adequately described by the "quasicircular" approximation. The quasicircular approximation holds when $Y \sin^2\theta/2(1-X)\cos\theta \ll 1$, where θ is the angle between the electromagnetic wave normal and the magnetic field vector, $X = (\nu_{pe}/\nu)^2$, and $Y = \nu_{Be}/\nu$; here, ν is the cyclic frequency of the wave. When the opposite inequality holds, the "quasiplanar"

(or "quasitransverse") approximation holds (Melrose 1980). In the former case, the radiation is very nearly circularly polarized and the Stokes I (total intensity) and V (circularly polarized radiation) parameters are the relevant observables. In the latter case, the radiation is linearly polarized at the source. However, Faraday rotation is very large in the coronal medium, and differential Faraday rotation across typical receiver bandwidths and/or the differential Faraday rotation from the front to back of an optically thin source washes out the linear polarization completely. There have been no modern reports of linearly polarized radio emission from flares.

MODE COUPLING Under some conditions, polarization observations and their interpretation are complicated by propagation effects. In general, the magnetoionic theory prevails and the electromagnetic wave modes propagate independently (weak mode coupling). If, in this case, the radiation traverses a region in which the longitudinal component of the magnetic field changes sign (quasitransverse region), the sense of circular polarization reverses. In contrast, in the limit of strong mode coupling, the magnetoionic theory breaks down and the magnetoionic modes are no longer strictly independent. Under conditions of strong mode coupling in a quasitransverse magnetic field region, the x-mode couples into the o-mode and vice versa. In such cases, the sense of circular polarization remains unchanged as the radiation traverses a quasitransverse magnetic field region (Cohen 1960). Mode coupling may also play a role in the depolarization of radio bursts. Zheleznyakov & Zlotnik (1963) show how a circularly polarized wave is converted to a linearly polarized wave when it traverses a quasitransverse magnetic field region; differential Faraday rotation then depolarizes the linearly polarized wave. More recent work has considered mode coupling in current sheets (Zheleznyakov et al 1996) and twisted magnetic field configurations (Melrose et al 1995).

SCATTERING OF RADIO WAVES IN THE SOLAR CORONA Microturbulence in the solar corona overlying a radio source can also modify the observed properties of radio emission from flares and associated radio bursts, as was first recognized by Roberts (1959) and subsequently borne out by detailed calculations by Fokker (1965) and Steinberg et al (1971), for the case of type I and type III bursts, respectively. Fluctuations in the refractive index in the turbulent plasma cause phase fluctuations in the propagating wave that result in a frequency-dependent blurring in radio maps. Bastian (1994) has pointed out that angular broadening is relevant to frequencies of several giga-Hertz (GHz) or more and therefore limits the angular resolution with which compact sources can be imaged at these frequencies. An important observational consequence of angular scattering, therefore, is that it prevents very high-angular resolution observations of solar

phenomena at radio wavelengths. Consequently prospects for solar very long baseline interferometry (VLBI) (Tapping et al 1983, Benz et al 1996b) are dim. Another possible consequence of angular scattering in the solar corona is the depolarization of radio bursts near the limb (Bastian 1995b).

3. CENTIMETER- AND MILLIMETER-WAVELENGTH EMISSIONS FROM FLARES

Centimeter- and millimeter-wavelength (cm-λ and mm-λ) emissions are from energetic electrons that are believed to carry a significant fraction, if not the bulk, of the energy liberated during the impulsive phase. In this section, we discuss how this energetic population of electrons manifests itself at cm-λ and mm-λ and how these emissions relate to X-ray and γ-ray emissions. We begin with a brief review of the instruments employed in recent years for the observations discussed. Because there has been considerable confusion in the literature about cm-λ source morphology and its relationship to optical and X-ray emissions, we ground the discussion in a schematic source model and show that it accounts for many of the observed properties of cm-λ sources. We then discuss the relationship of cm-λ emission to X-ray emission, cm-λ spectroscopy, and recent mm-λ observations.

3.1 *Instrumentation*

Beginning in the mid-1970s, production of high-resolution maps of cm-λ emission from flares became possible by using the Westerbork Synthesis Radio Telescope (WSRT; Baars & Hooghoudt 1974) and the Very Large Array (VLA; Napier et al 1983). The WSRT and the VLA are both general purpose (i.e. non–solar-dedicated) Fourier synthesis telescopes. The WSRT is a one-dimensional east-west array that has been used to observe flares in the 4.9-GHz band. The VLA is a multi-configuration two-dimensional (2D) array; hence, unlike the WSRT, it can provide time sequences of 2D "snapshot" maps of the evolving radio source. The VLA initially operated in the 1.4-, 4.9-, 15-, and 22.5-GHz bands. In the late 1980s, the 0.33- and 8-GHz bands were added. A major upgrade is planned for the VLA within the next decade, greatly improving its sensitivity, frequency coverage, and support of solar observing.

The RATAN 600 (e.g. Korolkov & Pariiskii 1979) is also used on an occasional basis to study radio emission from flares in one dimension with spectral coverage between $\approx$1 and 38 GHz and an angular resolution ranging from $18''$ at 15 GHz to $\approx 3'$ at 1 GHz. In recent years, the Siberian Solar Radio Telescope (SSRT) has provided observations of bursts in one or two dimensions at 5.7 GHz with an angular resolution of $\approx 15''$ (Altyntsev et al 1994).

The only solar-dedicated interferometric instrument in the United States is the Owens Valley Radio Observatory (OVRO) solar array. Formerly the OVRO

frequency-agile interferometer (Hurford et al 1984), the introduction of three additional antenna elements in 1991 provided a modest 2D imaging capability at up to 45 frequencies between 1–18 GHz (Lim et al 1994, Gary & Hurford 1994). Two antennas will soon be added to the OVRO solar array, yielding some much-needed improvement in its imaging capability.

The Nobeyama radioheliograph is an 84-element solar-dedicated array located in Japan (Nakajima et al 1994). Since the time it was commissioned, mid-1992, it has imaged the Sun at 17 GHz with an angular resolution of 10–20″ and a temporal resolution as high as 50 msec, although 1-sec time resolution is more typically employed. In November 1995, a 34-GHz imaging capability was added (Takano et al 1997), which produces 2D maps with an angular resolution of 5–10″, with a temporal resolution as high as 100 msec.

Interferometric observations of flares have been made by the Berkeley, Illinois, Maryland Array (BIMA) at Hatcreek, California, at a wavelength of 3 mm since 1989 (White & Kundu 1992). With the recent upgrade of BIMA to a nine-element, 2D array, mm-λ imaging is now possible (Silva et al 1996, 1997, Raulin et al 1997). The construction of the Millimeter Array in the coming decade will provide vastly improved sensitivity and imaging at mm-λ and sub–mm-λ thereby supplying important new opportunities to study the most energetic electrons in flares with a resolution and image fidelity far in advance of any instrument now available.

Spectral studies of impulsive flares at cm-λ have been carried out mostly by fixed frequency polarimeters operating at a number of widely spaced frequencies: Toyokawa, Nobeyama, Berne, and the US Air Force Radio Solar Telescope Network (RSTN); by single dishes equipped with broadband feeds and frequency-agile receivers (e.g. the new US Air Force solar radio burst locators); or an interferometer equipped with the same (OVRO; Hurford et al 1984).

3.2 *Centimeter-Wavelength Source Morphology and Kinematics*

One of the important lessons of soft X-ray (SXR) observations during the *Skylab* era was the recognition that magnetic loops constitute the basic "building blocks" of coronal structure (Rosner et al 1978) during both quiescence and flares (e.g. Pallavicini et al 1977, Kane et al 1980). Recognition of coronal magnetic loops as the building blocks of cm-λ sources is less obvious at first glance, a point that has resulted in much confusion in the literature in past years. Cm-λ source structure and polarization often change radically in appearance as a function of frequency and time. In some cases, more than one emission or absorption mechanism may play a role during a flare (Dulk et al 1986, Bastian & Gary 1992, Alissandrakis et al 1993). In others, propagation effects modify the polarization properties of the source. Nevertheless, the source morphology and

polarization of cm-λ emission from flares can often be qualitatively understood in terms of the dominant emission mechanism—gyrosynchrotron emission—acting within a coronal magnetic loop.

A SCHEMATIC MODEL To place the discussion on a more concrete footing, we first consider a magnetic loop configuration defined by two magnetic solenoids, A and B, of differing magnetic field strength embedded below the photosphere (Sakurai 1982). Solenoid A is -1000 G and has a radius of $5''$; solenoid B is $+500$ G and has a radius of $7.1''$. The two solenoids are separated by $20''$. We then consider a magnetic loop containing a nonthermal distribution of energetic electrons (Figure 1*a*). The distribution function of nonthermal electrons is a power law, $n(E)dE = n_\circ[(\delta - 1)/E_\circ](E/E_\circ)^{-\delta}dE$, with $\delta = 4$ and a low-energy cutoff $E_\circ = 10$ keV. The distribution is isotropic in pitch angle. The number density of energetic electrons on the axis of the magnetic loop with $E > E_\circ$ is $n_\circ = 5 \times 10^6$ cm^{-3}. The profile of $n(E)$ is a Gaussian perpendicular to the axis of the loop; the half-width of the Gaussian varies along the coronal magnetic loop as required by the field topology. The number density of background thermal electrons is $n_{th} = 3 \times 10^{10}$ cm^{-3}, assumed to be uniform throughout the source. The intensity and polarization were computed for 20 frequencies between 2–20 GHz, while assuming gyrosynchrotron radiation is the primary source of opacity. The effect of the background thermal plasma (Razin suppression) is included. Calculations similar to these have been performed by Preka-Papadema & Alissandrakis (1992). The results are summarized in Figure 1 *b–f*, where contour maps of 8 frequencies are shown. We note the following properties of cm-λ emission from the simulated coronal magnetic loop:

1. The source is optically thick to gyrosynchrotron self-absorption at low frequencies, tracing out the spatial extent of magnetic volume accessible to energetic electrons.

2. The source spectrum varies smoothly with frequency.

3. The source size decreases with increasing frequency. It is large and amorphous at the lowest frequencies and is composed of compact sources associated with magnetic footpoints at high frequencies.

4. The maximum brightness of the optically thick source lies between the magnetic footpoints A and B.

5. At intermediate frequencies, the loop top becomes optically thin, while the loop legs remain optically thick. At higher frequencies footpoint B becomes becomes optically thin and is less bright than footpoint A. At the highest frequencies both footpoints are optically thin.

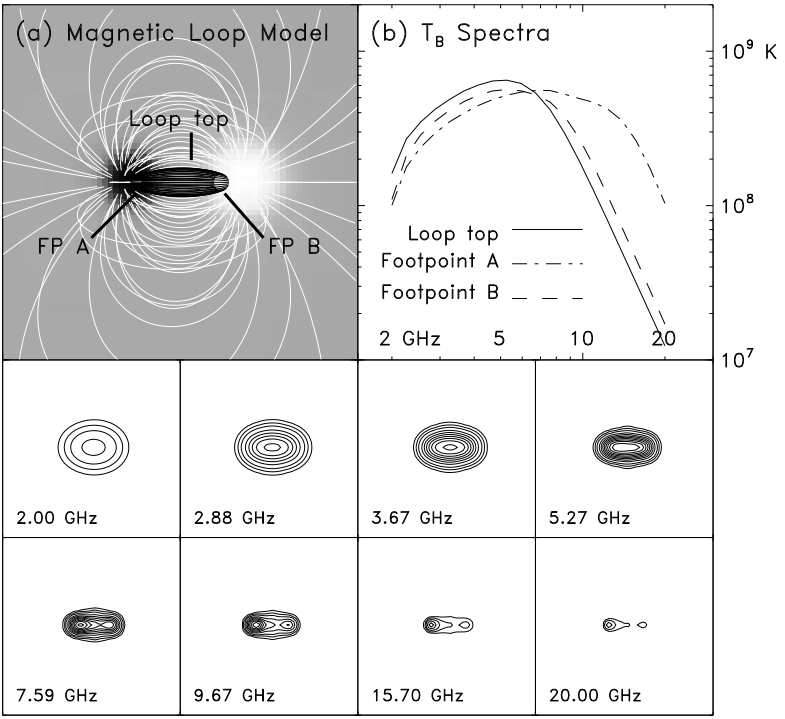

Figure 1 Gyrosynchrotron emission from a model coronal magnetic loop. *Top left*: A representation of the magnetic field lines of force. The *black lines of force* demarcate the full width at half maximum of the electron number density of nonthermal electrons. *Top right*: Brightness temperature spectra of the resulting gyrosynchrotron emission at magnetic footpoints A and B and at the loop top. In the *bottom two rows*, the brightness distribution of the Stokes I parameter are shown for eight frequencies. The *contour levels* are 2%, 5%, 10%, 20%, 30%, 40%, 50%, 60%, 70%, 80%, and 90% of 6.8×10^8 K. The scale of each of the *lower panels* is half that of the *upper-left panel*.

6. The spectra (Figure 1*b*) have a well-defined peak, ν_{pk}, that depends on location, as it is higher for the footpoints than at the loop top. Spectra at all locations become steeper below ∼2–3 GHz.

These points are easily understood. While it is well known that homogeneous source spectra can show harmonic structure at low frequencies, such structure is washed out here by inhomogeneities in the electron number density and, more importantly, by gradients in the magnetic field.

The overall source size decreases as a function of frequency owing to the inhomogeneity in both the number density of energetic electrons and the magnetic

field strength. Dulk & Dennis (1982) employed an inhomogeneous model to reconcile HXR and cm-λ observations. More recently, both direct and indirect observations have established the variation of the radio source size with frequency. Kocharov et al (1994) found more than an order of magnitude decrease in the full width at half maximum (FWHM)-source size over a factor of 10 in frequency for a flare observed in one spatial dimension. Other examples include Gary & Hurford (1990), Bastian & Gary (1992), and Kucera et al (1994). Typically, the characteristic source scale declines roughly as $d_{\rm FWHM} \propto \nu^{-1}$.

To understand the brightness distribution at each frequency, consider gyromagnetic emission by fully relativistic electrons. Electrons with energy $E = \gamma mc^2$ emit preferentially at a frequency $\nu \sim \gamma^2 \nu_{Be}$. Therefore, the energy of the electrons emitting at frequency ν is $E \propto (\nu/\nu_{Be})^{0.5} = s^{0.5}$, where s is the harmonic number. The mean energy of the emitting electrons can be expressed by the effective temperature $\langle E \rangle = k_B T_{\rm eff}$. For mildly relativistic electrons ($E \lesssim$ a few MeV), the dependence of the electron energy on s is somewhat steeper than for the ultrarelativistic case. For an isotropic power-law distribution of mildly relativistic electrons, we have, approximately, $T_{\rm eff} \propto s^{0.5+0.085\delta}$ (Dulk & Marsh 1982). A coronal magnetic loop is such that the field is strong at the footpoints and weaker at the loop top. If the loop is observed at a fixed frequency ν, the harmonic number s varies from a lower value at the footpoint to a higher value at the loop top. Therefore, higher energy electrons emit at the loop top, while lower energy electrons emit at the footpoint. In other words, a coronal magnetic loop behaves as a dispersive element, with different parts of the electron distribution function emitting at different locations within the magnetic loop.

When the entire magnetic loop is optically thick to gyrosynchrotron self-absorption, the observed brightness temperature $T_B \approx T_{\rm eff}$. At a given frequency, the maximum brightness from a nonthermal electron distribution is observed between the footpoints near the loop top, i.e. where the magnetic field is lowest and the energy of the emitting electrons is therefore highest. We note, however, that if the emitting distribution of electrons is purely thermal, an optically thick source has a uniform brightness temperature corresponding to the kinetic temperature of the emitting plasma. Examples of optically thick loop-top emission may be found in Shevgaonkar & Kundu (1985) and Bastian & Kiplinger (1991) (see also Figure 2). As $\kappa_\nu^{gs} \propto s^{-1.30-0.98\delta}$, the loop top becomes optically thin at a lower frequency than do the footpoints of the magnetic loop, and the footpoints dominate the observed brightness at high frequencies. In the case of an asymmetric magnetic loop, the magnetically weaker footpoint becomes optically thin at a lower frequency than does the magnetically stronger footpoint, and the magnetically stronger footpoint dominates the emission. Examples of footpoint sources are numerous (e.g. Shevgaonkar & Kundu 1985,

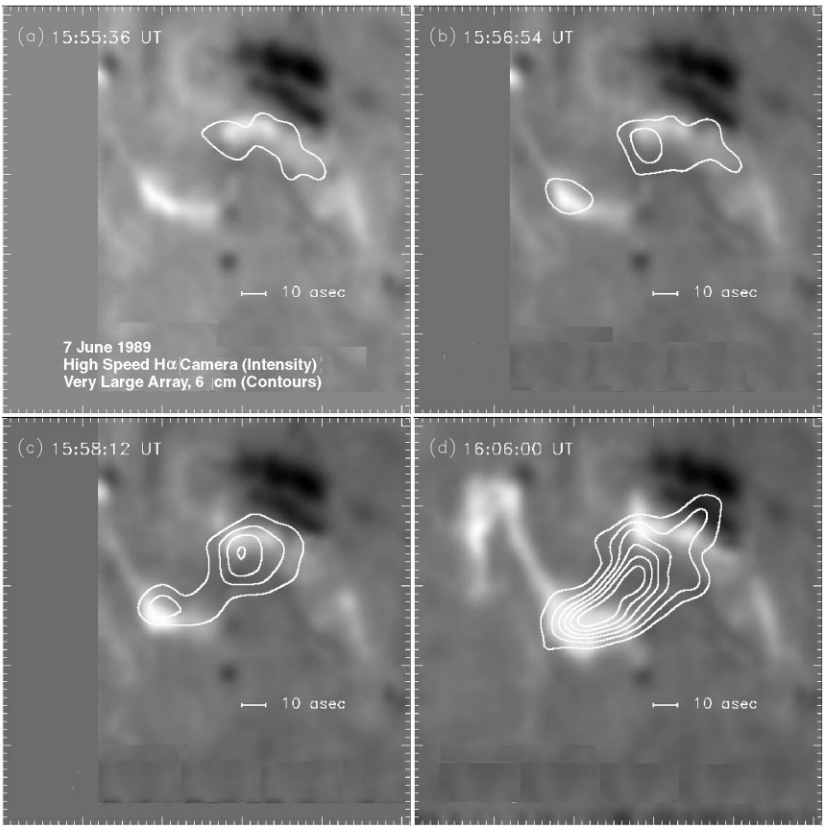

Figure 2 Example of the time evolution of a flaring source at cm-λ. The *contours* represent 4.9-GHz (λ = 6.1 cm) VLA observations of the M8.7 flare in AR 5528 studied by Bastian & Kiplinger (1991). The *gray scale image* shows the Hα emission, characterized by two ribbons. Large sunspots are seen to the northwest. (*a*) In the early phase of the flare, the region containing the strongest magnetic fields emits. (*b*) The magnetically conjugate footpoint then emits. (*c*) The 4.9-GHz emission bridges the magnetic neutral line. (*d*) The entire 4.9-GHz source is optically thick near the time of the flare maximum, and the location of maximum radio brightness lies between the magnetic footpoints.

Bastian & Kiplinger 1991, Alissandrakis et al 1993, Wang et al 1995, Kundu et al 1995a, Hanaoka 1996, 1997, Nishio et al 1997).

The polarization structure of the simulated coronal magnetic loop is not shown in Figure 1. At low frequencies, the source is very optically thick except at its edges, where the assumed number density of energetic electrons is small. The optically thick core of the inhomogeneous source is essentially unpolarized where θ, the angle between the wave normal and the magnetic field vector, is

large. In the optically thin "halo," and where θ is small, the source is polarized in the sense of the x-mode. At high frequencies, the source is optically thin and is polarized in the sense of the x-mode (Ramaty 1969). Observations confirm that high-frequency sources are generally polarized in the sense of the x-mode. Observations of optically thick sources tend to be unpolarized or polarized in the sense described above (e.g. Bastian & Kiplinger 1991, Gopalswamy et al 1995).

While simple loop models are useful for gaining a qualitative understanding of the source morphology at various frequencies, we must qualify the points made above with the following remarks. First, cm-λ sources are rarely single magnetic loops—they are generally composed of loop arcades (Figure 2), loops of widely differing scale (Figure 3), or more complex loop systems (Figure 4). Second, we have illustrated our points with a simple, isotropic, power-law distribution of energetic electrons of constant density along the magnetic loop. Thermal or hybrid electron distributions (Section 3.4) are possible, as are variations in the electron number density and/or anisotropy in the angular distribution of energetic electrons (e.g. Ramaty 1969). Each of these possibilities can result in different spectral and brightness distributions. Third, the source morphology can change radically as a function of time owing to a number of effects (see below). Fourth, as stated at the outset, complicating factors such as emission and absorption by mechanisms other than the gyrosynchrotron mechanism have been neglected. Free-free emission and absorption (Ramaty & Petrosian 1972) can play a role in certain flares, as can gyroresonance absorption (Dulk et al 1986, Alissandrakis et al 1993). Plasma radiation may contribute to the observed emission at frequencies below a few GHz (Section 4). Finally, propagation effects such as polarization reversals, depolarization, or angular broadening due to scattering (Section 2.2) have also been neglected. Nevertheless, the basic source structure of cm-λ sources can generally be understood in terms of gyrosynchrotron emission from ensembles of coronal magnetic loops containing energetic electrons.

Figure 3 Images of the GOES soft X-ray class C9.1 flare on April 10, 1993, in the National Ocean and Atmospheric Administration region 7469. Each image is $5.2' \times 3.9'$, with solar north to the top. (*a*) Total intensity (Stokes I) at 17 GHz. The resolution is indicated by the ellipse in the *upper right* of the panel; (*b*) circularly polarized flux (Stokes V); (*c*) SXT image near the time of flare maximum with microwave *contours* (*white*) and hard X-ray contours (*black*) overlaid; (*d*) SXT image during the decay phase; (*e*) a comparison of the microwave source (*contours*) with the photospheric magnetogram; (*f*) a schematic illustration of the magnetic loop configuration; (*g*) an Hα image of the flare; (*h*) the same as (*g*), but with a preflare image subtracted in order to reveal footpoint emission more clearly. (From Hanaoka 1997.)

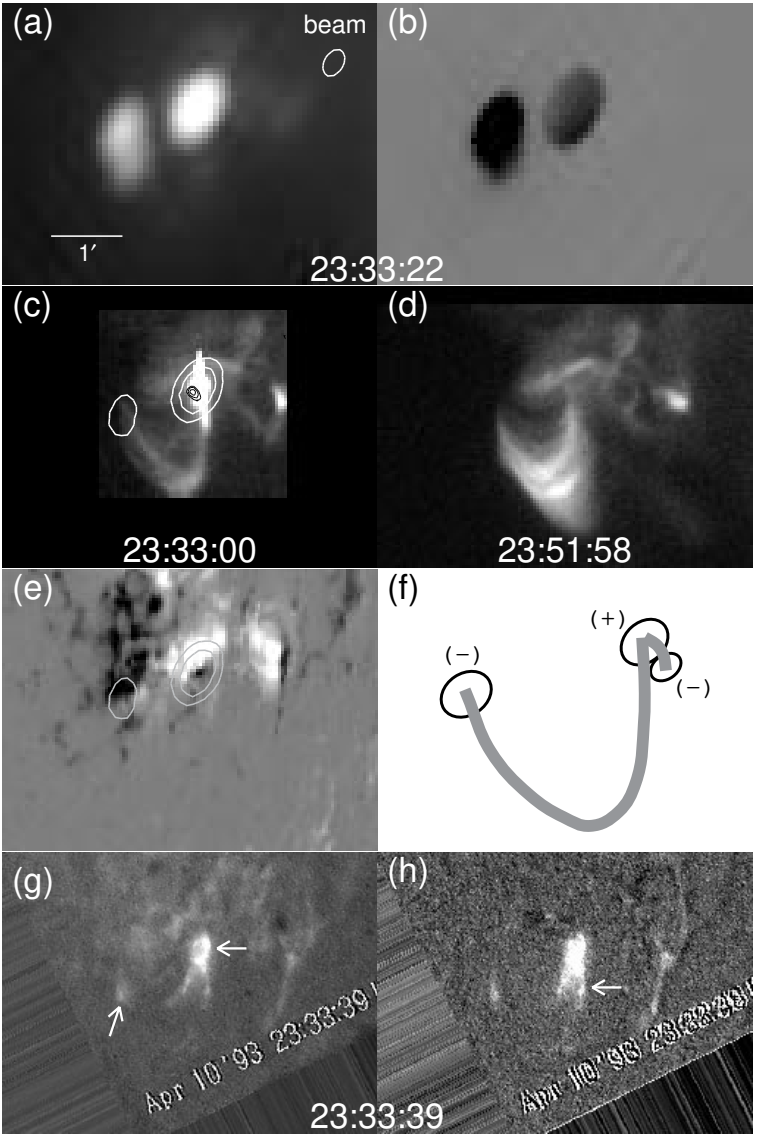
(a)
beam
1′
23:33:22
(b)
(c)
23:33:00
(d)
23:51:58
(e)
(f)
(+)
(−)
(−)
(g)
Apr 10 '93 23:33:39
23:33:39
(h)

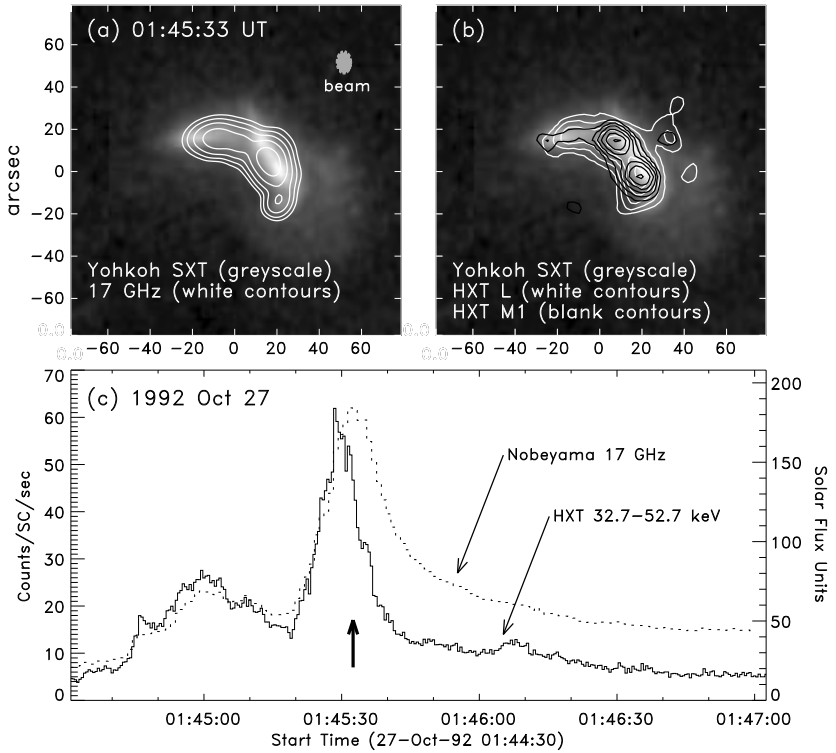

Figure 4 The M1.9 flare studied by Takakura et al (1994) involves a complex system of magnetic loops that fan out from a location to the south to several footpoints to the northeast and east. (*a*) The Nobeyama 17-GHz source (*contours*) overlies the Be 119 SXT image (*gray scale*) near the time of the flare maximum. The angular resolution of the 17-GHz map is indicated by the *ellipse* in the *lower-right corner*. (*b*) The HXT L channel (13.9–22.7 keV) emission (*white contours*) and the HXT M1 channel (22.7–32.7 keV) emission (*black contours*) overlie the SXT Be 119 image. (*c*) The time variation of the total 17-GHz emission and the HXT M1 channel. The time of the images shown in (*a*) and (*b*) is indicated by a *vertical arrow*.

TIME VARIATION OF SOURCE MORPHOLOGY While time sequences of high-resolution maps have been available for some time from the VLA and, more recently, the Nobeyama radioheliograph, the temporal evolution of cm-λ source morphology has received little attention, with the exception of preflare studies. Changes in the source morphology can occur when the optical depth along a given line of sight changes as the number density and/or energy distribution of energetic electrons varies. Alternatively, the dominant emission and/or absorption mechanism may change in the source or along the line of sight. Finally, the

source morphology can change because the magnetic field topology changes. The field topology can change as a result of the emergence of new magnetic flux, magnetic reconnection, or both.

An example of the first kind of time variation is illustrated in Figure 2. The GOES M8.7 flare of June 17, 1989, a two-ribbon LDE accompanied by a CME, was observed by the VLA at 4.9 GHz and by a high-speed Hα camera (Bastian & Kiplinger 1991). The source morphology changes radically with time: At the onset, only the most strongly magnetized footpoint (or footpoints) are seen to the northwest near a large sunspot group. The magnetically conjugate footpoints then radiate. Finally, the magnetic neutral line is bridged, and at the time of flare maximum, an arcade of coronal magnetic loops, optically thick at 5 GHz, bridges the two Hα ribbons. Studies of preflare activity have produced many examples of changing source morphology due to the emergence of magnetic flux and/or small magnetic reconnection events some time before impulsive energy release (Kundu et al 1982, Willson 1983, Shevgaonkar & Kundu 1985, Fujiki 1997).

3.3 *Comparison of Centimeter-Wavelength and X-Ray Source Properties*

The fact that time profiles of cm-λ and HXR emission are quite similar during flares was recognized long ago (Kundu 1961) (cf Figures 4 and 5), as was the correlation between flux levels in the two emissions (Arnoldy et al 1967, 1968) (Figure 6). The close correlation between cm-λ and HXR emission during flares has often been cited as evidence that the "same" population of energetic electrons is responsible for both types of emission. Is this the case? Are the numbers and energies of electrons required to account for HXRs and cm-λ emission consistent? Are the sources cospatial? Is there a detailed correlation in time? We now consider each of these questions.

ENERGY OF THE EMITTING ELECTRONS The energy of cm-λ–emitting electrons can be determined by direct or indirect means. A spatially resolved observation of an optically thick source yields a direct measurement of the mean energy of the electrons emitting at a particular frequency because $T_B = T_{\text{eff}} = \langle E \rangle / k_B$. While straightforward in principle, direct measurements have been infrequent in practice because, until recently, the only high-resolution 2D imaging instrument available for this purpose is the VLA. As the VLA is not solar-dedicated, the number of flares that have been observed at a suitable optically thick frequency (e.g. 5 GHz) is relatively small. Although a statistically robust sample is unavailable, published brightness temperatures span the range of a few times 10^7 K, corresponding to hot thermal plasma (Shevgaonkar & Kundu 1985, Kundu et al 1987, Schmahl et al 1990), to a few times 10^8 K (Kundu

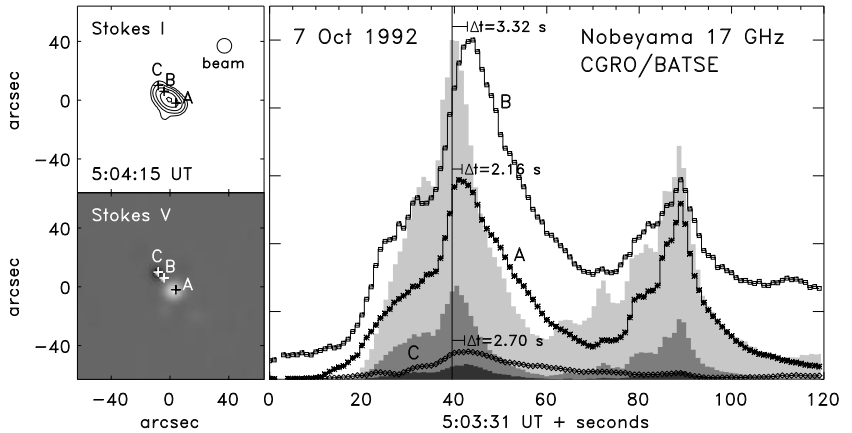

Figure 5 An example of the time variation of the Nobeyama 17-GHz brightness compared to the HXR count rate as measured by BATSE/CGRO for a simple magnetic loop. The *panels* to the *left* show a 17-GHz map at the time of the flare maximum. *Light curve B* shows Stokes I near the loop top. *Light curve A* shows Stokes V at the right-circularly polarized (RCP) footpoint; *light curve C* shows the absolute value of Stokes V for the left-circularly polarized (LCP) footpoint. The *gray-scale light curves* show the BATSE count rates in the 25- to 50-keV (*light*), 50- to 100-keV (*medium*), and 100- to 300-keV (*dark*) energy bins. *Light curves A* and *C* are scaled to *B*; HXR counting rates are scaled to the 25- to 50-keV count rate. The scaling is otherwise arbitrary. *Light curve B* (near the *loop top*) shows the largest delay relative to the 25- to 50-keV HXR count rate, while *A* (the RCP foot point) shows the smallest. *Light curve C* (LCP foot point) shows an intermediate delay. (See Bastian & Aschwanden 1998.)

et al 1981, Velusamy et al 1987, Bastian & Kiplinger 1991) to in excess of 10^9 K (Velusamy & Kundu 1982). Brightness temperature spectra have been obtained by the OVRO solar array in recent years (Gary & Hurford 1990, Lim et al 1994, Wang et al 1994, 1995, 1996, Belkora 1997, Komm et al 1998). Peak values of $T_{\rm eff}$ from these observations lie in the range $1–50 \times 10^7$ K, similar to the VLA results at 5 GHz. Excluding thermal sources, direct measurements of $T_{\rm eff}$ by the VLA and the OVRO solar array indicate electron energies of tens to >100 keV.

Given the practical difficulties associated with direct energy measurements, indirect methods have been employed using spatially unresolved measurements made by solar-dedicated instruments. These studies have all calibrated the energy of cm-λ–emitting electrons against HXR observations. Nitta & Kosugi (1986) exploited the well-known soft-hard-soft spectral evolution of the HXR spectrum during impulsive peaks (Kane & Anderson 1970, Kane et al 1980) to calibrate the energy of the cm-λ–emitting electrons, using a sample of flares observed by the *Hinotori* Hard X-Ray Monitor Spectrometer and the

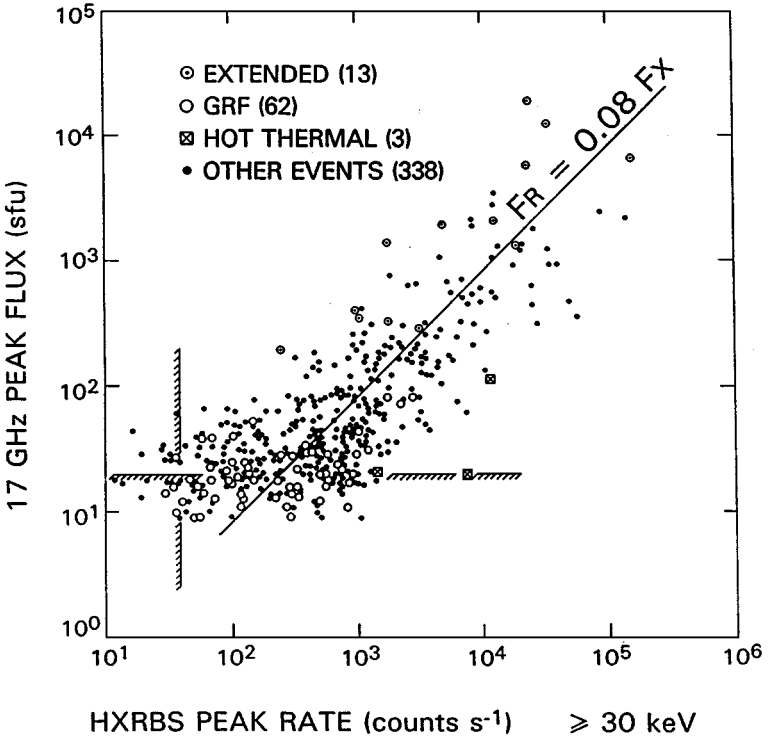

Figure 6 Scatter plot of the 17-GHz peak flux measured by the Nobeyama polarimeter versus the SMM/HXRBS (>30 keV) peak count rate. Impulsive flares, accounting for the vast majority, are indicated by *black dots*. The effective sensitivity thresholds of the two instruments are indicated by the *shaded lines*. (From Kosugi et al 1988.)

Nobeyama 17-GHz polarimeter. Assuming the HXRs are due to nonthermal thick-target bremsstrahlung emission, Nitta & Kosugi concluded that the 17-GHz emission was emitted by ∼130- to 180-keV electrons in magnetic fields of roughly 500–1000 G. Using HXR observations obtained by SMM Hard X-Ray Burst Spectrometer (HXRBS) and the 17-GHz polarimeter at Nobeyama, the peak 17-GHz flux was correlated with peak count rates measured in the HXRBS energy bands for a sample of impulsive flares and LDEs by Kosugi et al (1988). For impulsive flares, Kosugi et al found that the highest correlation is between 17 GHz and HXR peak fluxes for photon energies $\lesssim$80 keV, implying electron energies of $\lesssim$200 keV, consistent with the result of Nitta & Kosugi (1986). They infer a magnetic field strength of ∼900 G in 17-GHz impulsive sources. In contrast, they infer electron energies ∼1 MeV

and magnetic field strengths $\lesssim$100 G in 17-GHz LDE sources. Lu & Petrosian (1989) examined the ratio of 17-GHz fluxes measured by the Nobeyama polarimeter to HXR fluxes measured by the SMM/HXRBS. Good agreement between the observed and the calculated ratio was obtained for the rise phase for the thick-target model. Magnetic field strengths in the range of 350–750 G were inferred. The energy of the gyrosynchrotron-emitting electrons, assumed to be a power-law distribution with the spectral index obtained from the HXRBS observations, was again on the order of a few times 100 keV.

It is worth emphasizing that quantitative agreement between radio and HXR emission during the rise phase of impulsive flares, including the numbers of electrons required (Gary 1985, Lu & Petrosian 1989), is only possible if nonthermal, thick-target radiation dominates the HXR emission. We note that during the decay phase of impulsive flares, even the thick-target model is no longer strictly adequate, as the cm-λ and HXR decay at different rates (Lu & Petrosian 1989, Lee & Gary 1994; see below).

To summarize, a reasonably self-consistent picture based on direct and indirect observations has emerged. Electrons with energies of tens to perhaps a few times 100 keV produce cm-λ emission in impulsive flares. The "same" electrons are indeed responsible for both cm-λ and HXR emission to first order, although additional factors can complicate the situation, as we discuss in Section 3.2 and below. Magnetic field strengths in the range 300–1000 G are typically inferred. We note that at 17 GHz, this corresponds to a range of harmonic number $s \approx$ 6–20, somewhat lower than the canonical range of 10–100 typically assumed for gyrosynchrotron emission.

THE SPATIAL RELATIONSHIP OF CENTIMETER-WAVELENGTH AND X-RAY EMISSION Given that cm-λ and HXR emission are due to energetic electrons drawn from essentially the same distribution, it would seem that the spatial distribution of brightness in the two emissions would be closely related. However, progress in obtaining a detailed understanding of the spatial relationship between X-ray and cm-λ sources has been slow. The observational situation was still unclear little more than a decade ago (Vlahos et al 1986) owing to the dearth of simultaneous, high-quality cm-λ, SXR, and HXR imaging capabilities. This changed with the launch of the soft-X-ray telescope (SXT; Tsuneta et al 1991) and hard-X-ray telescope (HXT; Kosugi et al 1991), onboard *Yohkoh* in late 1991, and the availability of new or upgraded radio imaging instrumentation on the ground.

Observational progress on imaging nonthermal HXR emission from flares has been reviewed by Sakao (1994), Hudson & Ryan (1995), and Sakao et al (1996). HXR footpoint emission was first established by SMM/HXIS observations (Hoyng et al 1981, Duijveman et al 1982). Observations by the *Yohkoh*/HXT have extended and refined the results from SMM. Recent work

on nonthermal HXR (32.7–52.7 keV) emission from impulsive flares using the HXT (Sakao 1994) has established that the dominant HXR morphology is the double source, although single compact sources or multiple components are also frequently seen. Of the double sources for which magnetograms are available, the two sources lie on opposite sides of the magnetic neutral line. The time variation of the HXR flux in the two footpoints in double sources is coincident to $\lesssim$0.1 sec. Combined SXR, Hα, and imaging in a lower-energy HXR band (13.9–22.7 keV) establish double HXR sources as footpoint emission of flaring loops (Kosugi et al 1992, Sakao et al 1992). Of the two footpoints in double sources, the magnetically weaker footpoint is brighter in X-rays than is the magnetically stronger footpoint. These points are entirely consistent with the view that impulsive phase HXR emission is dominated by thick-target bremsstrahlung emission by nonthermal energetic electrons and exclude protons or thermal conduction fronts as the primary source of HXR emission (Sakao 1994). Given that HXR emission is dominated by radiation from magnetically conjugate footpoints, and that SXR emission outlines the footpoint connectivity, a close morphological correspondence might be expected between cm-λ and X-ray sources, in addition to the flux correlations pointed out previously. This is indeed the case, although some important qualifications are necessary.

Wang et al (1995) obtained images of an impulsive flare with the OVRO solar array, the SXT, and the HXT and found that (*a*) SXR emission connected two footpoints; (*b*) the HXR emission was associated with one footpoint; (*c*) the cm-λ emission was concentrated in the other footpoint. Wang et al found that the footpoint associated with the cm-λ source was more strongly magnetized than that associated with the HXR source. This result is in qualitative agreement with the HXR results of Sakao (1994) and the schematic loop model presented in Section 3.2. In an asymmetric coronal magnetic loop, the more strongly magnetized footpoint preferentially emits cm-λ radiation, while HXRs are preferentially associated with the weaker footpoint because the mirror point of the electrons is lower and electrons precipitate from the magnetic loop in greater numbers there. A similar result was reported by Kundu et al (1995a), who compared HXR and 17-GHz images obtained by the HXT and the Nobeyama radioheliograph, respectively.

More comprehensive studies of X-ray/cm-λ source morphology have been carried out by Hanaoka (1996, 1997) and by Nishio et al (1997). Nishio et al found that the majority of impulsive flares in their sample (10 of 14) involve at least two coronal magnetic loops or loop systems. Typically, one loop system is compact ($\leq$20″), while the other is larger (30″–80″). Both loops have 17-GHz emission, and the time variation of the 17-GHz flux is similar in both. These characteristics agree with earlier observations of primary and secondary source

structure (Nakajima et al 1985, Gary & Hurford 1990, Wang et al 1996). HXRs are preferentially detected from the more compact of the two loops, although remote HXR components are also occassionally seen (Kosugi 1994). Similarly, SXR emission is brighter in the compact loop, although it is also detected in the larger loop. Hanaoka (1997) has studied the "double-loop configuration" explicitly. He found that the configuration usually arises from the emergence of a parasitic magnetic polarity within the leading or following part of an active region. An example is shown in Figure 3, where a compact loop to the west oriented roughly north-south (as determined by the gradient in circular polarization) interacts with a large-scale loop oriented east-west. Both Nishio et al and Hanaoka concluded that double-loop configurations play a role in the majority of impulsive solar flares.

To summarize, recent observational results have clarified the spatial relationships among cm-λ, SXR, and HXR sources. The emissions are spatially and temporally well correlated. SXR emission demarcates coronal magnetic loops of hot, dense, thermal plasma. The dominant sources of HXR emission are in conjugate magnetic footpoints in the low corona. Cm-λ emission traces out the entire volume accessible to nonthermal electrons. Footpoint emission dominates at high frequencies. Asymmetric magnetic loops yield stronger HXR emission at the magnetically weak footpoint, whereas the magnetically stronger footpoint dominates high-frequency cm-λ emission, leading to a displacement between the dominant HXR and cm-λ sources. Recent studies of cm-λ source morphology suggest that impulsive flares commonly involve loop-loop interactions—both a compact and a larger-scale magnetic loop structure interact due to new flux emerging into preexisting magnetic structures.

THE RELATIVE TIMING OF CENTIMETER-WAVELENGTH AND HARD X-RAY EMISSION While there is a close correlation between HXR and cm-λ emission flux and time variation, the two emissions often differ in detail. Timing comparisons made with spatially unresolved HXR counting rates and radio fluxes invariably find that temporal features in cm-λ emission (e.g. the time of maximum flux) lag behind those in HXRs by 1–3 sec (Crannell et al 1978, Starr et al 1988; cf Figures 4 and 5). Furthermore, the cm-λ emission typically decays more slowly than the HXR count rate. Kaufmann et al (1983) and Cornell et al (1984) compared multiple fine structures in flares by filtering out the slowly varying component of the HXR and radio flux. They both found that discrete fine structures are more tightly correlated and that the magnitude of the cm-λ lag is 200–300 msec, an order of magnitude smaller than that obtained for total flux comparisons. On this basis, Lu & Petrosian (1990) identified two time scales in the problem: a short time scale associated with HXR/cm-λ fine structure and a longer time scale (factor of $\sim$10) associated with the total flux variation.

Bastian & Aschwanden (1998) have examined a sample of flares observed jointly by the Nobeyama radioheliograph at 17 GHz and the BATSE instrument on board the *Compton Gamma Ray Observatory* (CGRO). When compared as spatially unresolved emissions, the HXR/cm-λ timing agrees with previous analyses. However, unlike past timing comparisons, the radioheliograph provides temporally and spatially resolved observations. Timing comparisons are therefore possible between the nonthermal thick-target (footpoint) HXR emission and the cm-λ emission at various locations within the source. When specific lines of sight are considered, the mean cm-λ delay can vary considerably within a given source. Invariably, footpoint emission at cm-λ shows the minimum delay relative to HXRs, while loop-top sources show the largest delays (Figure 5). The variation of delays within a single flare can be largely attributed to energy-dependent effects. As noted in Section 3.2, a magnetic loop acts as a dispersive element—emission at a fixed frequency from locations where the field is weak comes from more energetic electrons than for locations where the field is strong. Hence, any mechanism that modifies the electron energy distribution in an energy- and time-dependent manner will also modify the relative timing of emission from various source locations.

One or more mechanisms may be involved in the delay of cm-λ emission relative to HXRs. Lu & Petrosian (1990) found that in the case of electrons injected into a convergent magnetic geometry, transport effects can delay the cm-λ emission relative to the HXRs by $\lesssim$200 msec. Hence transport effects might be relevant to the smallest delays observed. Alternatively, or in addition, electron trapping may account for the full range of delays observed (e.g. Kaufmann 1983, Cornell et al 1984, Dennis 1988, Aschwanden et al 1997, Bastian & Aschwanden 1998). High-energy electrons have a longer lifetime against Coulomb collisions than low-energy electrons and are therefore scattered into the loss-cone less frequently than low-energy electrons. High-energy electrons therefore remain in the magnetic trap for a longer time, and the radiation they emit peaks later than the HXRs, which are due to precipitating electrons only. Another possibility is that higher-energy electrons are simply accelerated somewhat later than lower-energy electrons (so-called "second-step" acceleration models; e.g. Bai & Ramaty 1979, Bai & Dennis 1985). Trapping and/or delayed acceleration may also account for the differences in HXR and cm-λ decay times to which we alluded above.

3.4 *Centimeter-Wavelength Spectroscopy of Flares*

In principle, the broadband cm-λ spectrum is a powerful diagnostic of physical conditions in flares. In practice, there are difficulties in exploiting it as such. The most important one is that, until relatively recently, there has been no instrument capable of providing spatially resolved cm-λ spectra. As shown

in Section 3.2, cm-λ source morphology can vary radically as a function of frequency. Spatially resolved spectroscopy is therefore essential for obtaining meaningful radio spectra. However, most work to date has interpreted spatially unresolved spectra in terms of simple, homogeneous models. We therefore briefly discuss spatially unresolved spectroscopy before going on to recent work in the fledgling field of imaging spectroscopy.

SPATIALLY UNRESOLVED SPECTROSCOPY The spectrum of most impulsive flares is characterized by an inverted "U" morphology at cm-λ, usually peaking at a frequency $\nu_{pk} = 5$–10 GHz (Guidice & Castelli 1975, Wiehl et al 1985, Cliver et al 1985, Stähli et al 1989). Roughly 20% show a dm-λ tail extending up to ∼3 GHz. Early studies showed that only ≈5% of the observed spectra show more than one spectral component. In contrast, using a sample of flares observed between 1–18 GHz with a spectral resolution of ≈6%, Stähli et al (1989) found that most impulsive flares show more than one spectral component,[3] which they attribute to the superior spectral resolution of the study. For the main spectral component, Stähli et al (1989) found the following. 1. The low-frequency slope of the (optically thick) spectrum is $\alpha > 3$ for $\gtrsim$40% of the flares observed. Extreme values ($\alpha > 6$) are observed for ∼10% of the flares. 2. The turnover frequency ν_{pk} remains remarkably constant throughout the development of the flare for the majority. 3. The average spectral bandwidth of the cm-λ spectra was 80–95%.

For a homogeneous source, $T_B(\nu) \propto \nu^{2.5+0.085\delta}$ (Dulk & Marsh 1982) and the spectral bandwidth is $\lesssim$75%. Source inhomogeneity can only make spectral slopes shallower and the spectral bandwidth larger. While larger spectral bandwidths are indeed observed, in general, how can we account for the large spectral indices observed for the optically thick emission from many flares? At least four ways have been considered: (*a*) Razin suppression (Klein 1987, Belkora 1997), which suppresses emission from frequencies below the Razin-Tsytovich cutoff frequency $\nu_{RT} \approx 20 n_e / B$ Hz; (*b*) free-free absorption (Klein 1987) or gyroresonance absorption (Dulk et al 1986) along the line of sight; (*c*) thermal gyrosynchrotron absorption by the ambient plasma (Benka & Holman 1992); (*d*) emission at significantly lower harmonics (3–10) than supposed by Dulk & Marsh. Of these, Razin suppression has the additional advantage that it may also account for the constancy of ν_{pk}, although a high ambient density ($n_{th} \gtrsim 10^{11}$) is required.

[3]Regarding the secondary spectral components reported by Stähli et al (1990), an instrumental effect was later discovered at OVRO (a third-harmonic response of the front-end mixer) that could cause spurious low-frequency components at ≈10% of the peak flux of the main component. Thus, the fraction of bursts with secondary or multiple components is likely to be significantly lower than the 80% found by Stähli et al. The conclusions regarding the properties of the main spectral component remain valid, however.

Benka & Holman (1992) consider broadband cm-λ spectra within the context of a specific model for plasma heating and electron aceleration, the "thermal/nonthermal" (TNT) model for radio bursts. The TNT distribution results from Joule heating and electron acceleration in quasistatic DC electric fields. Benka & Holman (1992) suggested that the near constancy of ν_{pk} may reflect the systematic evolution of the electric field during the course of a flare. They were able to fit a complex OVRO spectrum to a homogeneous TNT source model. Unfortunately, the spectral structure to which they fit must be regarded as suspect (see footnote), and while the TNT model is attractive for a number of reasons (see Section 6), the spectral complexity that it predicts is expected to be smoothed out in real sources due to gradients in the electron number density and, more importantly, the magnetic field (Section 3.2).

More than half of the flares observed by Stähli et al (1989) do not have steep low-frequency slopes. Indeed some show spectra in the opposite extreme. Lee et al (1994) discussed a class of cm-λ bursts that have very flat spectra in their late stages over the entire range of 1–18 GHz. These bursts were X-class in SXRs and had extremely high cm-λ flux densities of $\gtrsim 10^4$ sfu. Lee et al concluded that such spectra are due to sources of extreme inhomogeneity, in which the low-frequency source is as large as $300''$, while at higher frequencies the source is much smaller. Other examples of flat-spectrum sources include those studied by Ramaty & Petrosian (1972), where the flat spectrum was attributed to the dominance of thermal free-free absorption in the source function.

IMAGING SPECTROSCOPY A spatially unresolved spectrum represents a weighted average over a (possibly) complex brightness distribution (cf Figures 2–4). The changing brightness distribution as a function of frequency can severely bias any quantity derived from the spatially integrated spectrum coupled with naive assumptions about the source morphology. To avoid these problems, it is necessary to obtain well-resolved images of the source at many frequencies to form brightness temperature spectra directly. Brightness temperature spectra can then be interpreted in a more robust fashion.

Only two instruments can obtain spatially resolved broadband spectroscopic data: the OVRO Solar Array and the RATAN 600. Unfortunately, both have significant imaging limitations. The RATAN 600 is a transit instrument and therefore observes flares only rarely (e.g. Bogod et al 1990). Furthermore, it can only image them in one dimension. The OVRO Solar Array has obtained images of many bursts, but because of the small number of antennas (five), imaging is limited to rather simple source structure.

Despite these limitations, the utility of brightness temperature spectra is already clear. For example, both radio and HXR spectra should yield the index of a power-law distribution of energetic electrons in a flare, yet past observations

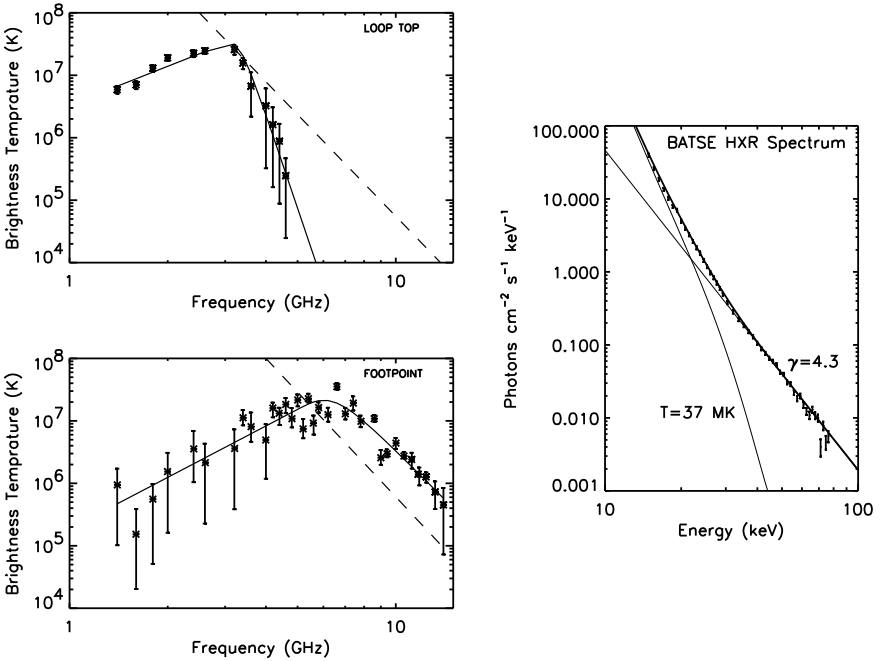

Figure 7 Maps at 34 frequencies from the OVRO Solar Array (after Wang et al 1994) were used to obtain these brightness temperature spectra (*left-hand panels*) at two points in a flaring loop. The *upper-left panel* corresponds to the top of the flaring loop, while the *lower-left panel* corresponds to one footpoint. The *right-hand panel* (R Schwartz, private communication) shows the BATSE HXR photon spectrum accumulated over the same time, with a two-temperature plus power-law fit overlaid. The electron power law distribution that accounts for the HXR photon power-law spectrum should give a gyrosynchrotron spectral slope given by the *dashed line* in the *left-hand panels*. The position of the dashed line is arbitrary—only the slope is relevant. The footpoint radio spectrum agrees well with this prediction, while the loop-top radio spectrum is consistent with thermal gyrosynchrotron emission near 30 MK, as discussed by Wang et al (1994).

based on spatially unresolved radio spectra (e.g. Marsh et al 1981) have failed to find agreement. When spatially resolved T_B spectra are used (Wang et al 1994, 1995), they are indeed consistent. Figure 7 shows brightness-temperature spectra obtained by the OVRO Solar Array for loop-top and footpoint locations in a flaring magnetic loop (cf Figure 1*b*). The HXR spectrum from the BATSE instrument on the CGRO indicates a hot thermal component with a temperature of 3.7×10^7 K and a component with a power-law photon index of $\gamma = 4.3$. For thick-target HXR emission, the index of a power-law distribution function is $\delta = \gamma + 1 = 5.3$, which yields the expected radio

spectral slope for gyrosynchrotron emission. The observed spectral slope of the footpoint source agrees well. Interestingly, the loop-top spectrum falls off far more steeply at high frequencies than does the footpoint spectrum. Wang et al (1994) suggested the loop top is dominated by thermal gyrosynchrotron emission at a temperature of about 3×10^7 K, in rough agreement with the BATSE hot thermal component. Other examples of images and brightness temperature spectra appear in Wang et al (1995, 1996) and Komm et al (1998).

To summarize, broadband imaging spectroscopy is required for quantitative analysis of flares. While the imaging capabilities of existing spectroscopic instruments need improvement, they nevertheless suffice to show the potential power of the technique (Figure 7).

3.5 *Millimeter-Wavelength Emission from Flares*

While significant progress has been made in imaging HXR emissions with the *Yohkoh* HXT, no imaging capability exists for photon energies $\gtrsim$100 keV. Cm-λ emission results from electrons with energies of tens to hundreds of keV. Gyrosynchrotron radiation at mm-λ is of particular interest because it is produced by electrons with energies $\gtrsim$1 MeV (White & Kundu 1992). Hence, mm-λ observations offer access to some of the most energetic electrons produced in flares, those that place some of the greatest demands on acceleration mechanisms.

Observational work at mm-λ has proceeded along two lines. First, using polarimeters at one or more sites, light curves of the spatially integrated flux have been studied at fixed frequencies between 35–80 GHz. Early observations showed that some flares have an apparent spectral flattening at mm-λ, which Kaufmann et al (1986) attribute to an additional high-frequency spectral component. Correia et al (1994) showed that flat and rising spectra at mm-λ are more common than was previously suspected. Chertok et al (1995) argued that the flat mm-λ component of at least some flares can be attributed to optically thin thermal free-free radiation from warm (but less than SXR-emitting temperatures) dense plasma evaporated from the chromosphere. Pohjolainen et al (1996) found that most impulsive flares (87%) show evidence for thermal free-free emission, usually as a post-burst increase.

Other flares, however, clearly involve a distinct population of nonthermal electrons at high energies, separate from that producing cm-λ and HXR radiation (Lim et al 1992, Kundu et al 1994, Vilmer & Trottet 1997). Spectral hardening at high energies has also been noted in photon spectra observed by the SMM and *Hinotori* missions (e.g. Bai & Dennis 1985, Dennis 1988, Yoshimori 1989). Joint HXR/mm-λ observations are very few in number. Two examples, observed in HXRs by the PHEBUS instrument on GRANAT and the

Berne polarimeters, clearly showed the presence of a distinct, hard, nonthermal component in HXRs above a break energy of ≈500 keV that is responsible for the mm-λ emission. Vilmer & Trottet (1997) pointed out that the spectral ratio of 19.6- to 35-GHz emission was sensitive to the presence of the hard component when HXR counting statistics were too low to detect its presence.

A second line of observational work at mm-λ has been undertaken only recently: spatially resolved observations of flares with BIMA. Interferometric observations of the mm-λ emission offer the most direct means of determining when and where MeV electrons are present in flares. The BIMA observations are far more sensitive to impulsive mm-λ emission than polarimeters because an interferometer filters the signal from the background Sun from its response. Hence, events of a fraction of a solar flux unit commonly have been seen. The BIMA observations show the following: 1. Flares of all sizes produce MeV electrons on prompt time scales. 2. In agreement with fixed frequency polarimetric studies, MeV electrons often appear to form a distinct population of fast particles from the cm-λ/HXR-producing electrons. The first of these results is a surprise. Bai & Sturrock (1989) distinguished between nonthermal (impulsive) HXR flares and impulsive γ-ray/proton (GR/P) flares. The latter are accompanied by prompt acceleration of electrons to relativistic energies and protons to γ-ray–producing energies. The fact that most impulsive flares are accompanied by mm-λ emission may render the distinction unnecessary: All impulsive flares may accelerate electrons and ions to relativistic energies. Impulsive GR/P flares may only represent the extreme tail of the distribution.

To summarize, spatially unresolved spectroscopic observations and single-band interferometric observations have shown that while the majority of impulsive flares are accompanied by thermal free-free emission at mm-λ, many, if not all, flares also show the presence of a nonthermal population of energetic electrons that is distinct from those producing cm-λ and HXR emission.

4. DECIMETER- AND METER-WAVELENGTH EMISSION FROM FLARES

Radio emission associated with flares at m-λ and dm-λ differs significantly from that at cm-λ and mm-λ. This is because incoherent gyrosynchrotron radiation gives way to coherent plasma radiation and possibly other emission mechanisms below frequencies of 1–3 GHz. This is largely a function of the electron number density in, and above, active regions: For electron number densities of $n_e = 5 \times 10^8$–10^{11} cm^{-3}, which is the range expected, the electron plasma frequency is ≈200 MHz to 3 GHz. It is therefore within this frequency range that plasma radiation is most commonly observed. At the same time, gyrosynchrotron radiation tends to be strongly self-absorbed and falls off steeply

with decreasing frequency. Free-free absorption also tends to absorb incoherent emission from low-lying layers.

A descriptive summary of m-λ radio bursts has appeared in these volumes previously (Dulk 1985). A more detailed and comprehensive account may be found in a volume edited by McLean & Labrum (1985) or by Melrose (1980). Recent work at m-λ and dm-λ has focused on the observational manifestations and diagnostic uses of electron beams in the solar corona (type III and type III–like bursts), on narrowband spike bursts, and on the relation of classical radio bursts to coronal structures as revealed by SXR imaging.

4.1 *Instrumentation*

The instrumentation used to explore the dm-λ/m-λ includes fixed frequency polarimeters (e.g. the US Air Force/RSTN network), spectrographs, and radioheliographs. The Culgoora radioheliograph and the Clark Lake Radio Observatory (CLRO) were closed in the mid-1980s, leaving only the Nançay radioheliograph and the VLA to image dm-λ/m-λ phenomena. The VLA, described briefly in Section 3.1, supports two frequency bands in the dm-λ/m-λ regime: 300–350 MHz and 1250–1700 MHz. The Nançay radioheliograph has recently been upgraded (Kerdraon & Delouis 1997) to provide dual-polarization (I and V) 2D imaging at frequencies between 150–450 MHz and an angular resolution that varies between 40″–2′ east-west and roughly 1.8′–5.5′ north-south. It is worth noting that the VLA has recently added support of the 74-MHz band, and the Giant Meterwave Radio Telescope (near Pune, India; Swarup 1990) will soon be operational, thereby recovering some of the m-λ imaging capabilities lost with the closures of Culgoora and the CLRO.

The status of spectrographs operating at dm-λ and m-λ has been reviewed by Krüger & Voigt (1995). These include the PHOENIX spectral polarimeter at Bleien, operated by the ETH/Zürich (Benz et al 1991) between 100 and 3000 MHz; the ARTEMIS multichannel spectrograph (Dumas et al 1982), operating between 100 and 469 MHz (recently moved from Nançay to Greece); and the four survey sweep spectrographs at Tremsdorf operating between 40 and 800 MHz.

4.2 *Radio Emission from Electron Beams*

Fast drift radio bursts, or type III bursts, were among the first types of m-λ bursts discovered in the 1940s. The drift of the emission to lower frequencies with time was interpreted by Wild (1950) as the signature of a particle beam propagating upward through the corona at a speed ~ 0.2–$0.6c$. Later, occasional reverse-drift bursts were discovered (downward-directed beams), as well as bursts that first decrease, and then increase, with frequency (U bursts, due to electron beams propagating in a closed magnetic loop). Summaries of the early observations

can be found in Krüger (1979), Suzuki & Dulk (1985), and Pick & van den Oord (1990).

Currently, type III bursts are the most important and useful coherent bursts because their physics is at least qualitatively understood. Accordingly, the recent interest in type III bursts in the solar corona is motivated by their use as a diagnostic of the acceleration process of electrons in flares, as tracers of the magnetic field lines along which the beams propagate, and of the ambient density along their trajectory.

It is generally agreed that energetic electrons produce type III emission in three basic steps.

1. Beam formation: If the acceleration process does not intrinsically produce a beam, propagation eventually will. As particles propagate along magnetic field lines, the fastest ones will arrive at a remote location first, where they constitute a "bump on the tail" of the ambient electron distribution.

2. Plasma instability: As soon as a significant positive gradient in velocity space develops—beyond about three times the thermal velocity of the ambient electrons, v_{te}—the "bump-on-tail" instability sets in and plasma waves grow exponentially. They are approximately electrostatic Langmuir waves with a phase velocity equal to the particle velocities of positive gradient. The frequency of the Langmuir waves is slightly above the value of ν_{pe} in the ambient medium. The distance Δz required for the electron distribution first to become unstable to the production of Langmuir waves depends on how rapidly the acceleration and heating occur, i.e. on the e-folding acceleration time τ. For a Maxwellian distribution at the acceleration site, $\Delta z \approx 27(v_{te}/v_{th})^2 v_{te}\tau$, where v_{th} is the thermal velocity of the hot electrons (Benz 1993). The expression for Δz demonstrates that unstable beams form after a few thousand kilometers for acceleration times less than one second.

3. Wave conversion: The Langmuir waves are transformed into transverse electromagnetic waves with frequencies near the fundamental of the local plasma frequency, ν_{pe}, or its harmonic, $2\nu_{pe}$. The dominant emission process at ν_{pe} remains controversial. For interplanetary type III bursts, the most significant process, as determined by in situ measurements, is the decay of the Langmuir wave into a daughter Langmuir wave and an ion sound wave ($L \Rightarrow L' + S$). The ion sound wave then coalesces with a Langmuir wave into a radio wave ($L + S \Rightarrow T$). The direct decay into transverse waves ($L \Rightarrow L' + T$) does not appear to be a major process (Lin et al 1986). Quantitative agreement between observations and a linear radiation theory has now been reached (e.g. Cairns & Robinson 1995). Whether these processes produce coronal type III bursts, however, remains to be seen. In

the case of harmonic plasma radiation, it is widely accepted that a transverse wave is produced with a frequency of $\approx 2\nu_{pe}$ when two Langmuir waves, each with a frequency near ν_{pe}, coalesce ($L + L' \Rightarrow T$).

HIGH-FREQUENCY TYPE III BURSTS Initially, type III or type III–like radio bursts were not expected at frequencies above a few times 100 MHz. This is because free-free absorption of plasma emission from the plasma frequency layer increases strongly with frequency. Because the density increases downward, the local plasma frequency increases. It was therefore taken for granted that coherent plasma radiation from the bulk of downward-directed electron beams accelerated in flares, if it occurred at all, was invisible because of strong free-free absorption. Nevertheless, early observers of the long-wavelength part of the dm-λ range noted type III–like bursts that did not continue into the m-λ range (Young et al 1961). With higher time resolution, some of these bursts were later classified as "pulsations" of the type IV burst continuum. Others, however, turned out to drift with values of $\dot{\nu}/\nu$ comparable to m-λ type III bursts. This was also the case for the roughly 100-MHz wide "blips" first found in association with weak gyrosynchrotron emission at 5 GHz (Benz et al 1981, Fürst et al 1982). A critical difference between the drifts seen in blips and m-λ type III bursts is the sense of the drift: 90% of the blips studied by Benz et al (1983) drifted from low to high frequencies, which is opposite to the drift of type III bursts. However, the magnitude of observed drift rate suggests an exciter speed of about $0.3c$, and the duration follows the ν^{-1} law derived for type III bursts in the m-λ and kilometer-wavelength ranges. Thus blips and similar bursts at wavelengths shorter than m-λ have come to be called "decimetric type III bursts," or type IIIdm bursts; they are assumed to be caused by downward-directed electron beams (Figure 8). In the 1- to 3-GHz range, the type IIIdm bursts are the most frequently observed coherent radio emission (Isliker & Benz 1994a). Occassionally, type III–like bursts extend to even higher frequencies, as they have been detected at 3.5 GHz (Stähli & Benz 1987) and 8.5 GHz (Benz et al 1992)! In most of the events, the spectral drift again indicates downward motion in the corona.

Thus, contrary to early expectations, type III–like phenomena are observed through the dm-λ range into cm-λ. How can the dm-λ and cm-λ type III bursts be observed in the presence of ferocious free-free absorption? It is likely that two factors allow the escape of such radiation. 1. The bursts are due to harmonic plasma radiation, so the free-free absorption is less severe. 2. The radio sources must be located in overdense structures, presumably flux tubes with large horizontal density gradients along which the radiation can escape into a low-density medium (Aschwanden et al 1985, Benz et al 1992). In other words, the effective scale height Λ is very small due to the fibrous, highly inhomogeneous nature of the solar corona.

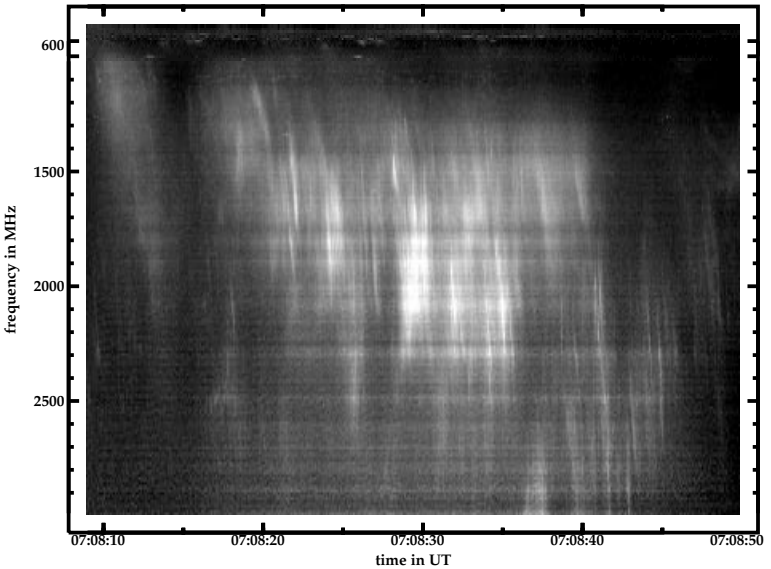

Figure 8 Example of decimetric type III bursts from Isliker & Benz (1994a). The spectrogram shows enhanced emission (*bright*) in the frequency-time plane. More than a hundred bursts are discernible, all moving from low to high frequency and thus downward in the corona.

TEMPORAL CORRELATION OF TYPE III BURSTS WITH HXRS Only 3% of m-λ type III bursts are correlated with impulsive HXR emission (Kane 1981), although the correlation increases with increasing type III start frequency and with intensity. Since m-λ type III bursts mostly propagate upward, it is perhaps not surprising that those originating high above active regions are poorly correlated with HXR events. Aschwanden et al (1985) showed that 48% of reverse-drift type IIIdm bursts are correlated with HXR bursts, consistent with the expectation that downward-directed electron beams should correlate better with thick-target HXR emission than upward-directed beams. Using higher quality radio-spectroscopic data around 300 MHz, Aschwanden et al (1995b) studied sequences of correlated HXR and classical type III bursts with equal burst durations and intervals in all strong flares. They concluded that there is a causal relation between the upward-directed beams of electrons producing type III bursts and the downward-directed beams of electrons producing HXR pulses and that the two emissions are related through the production of bidirectional electron beams by the acceleration process.

Nevertheless, it is clear that not every HXR peak is associated with a type III or type III–like radio burst. Aschwanden et al (1995a) found an associated type

III burst in 31% of individual HXR pulses. What determines whether or not a given downward-moving electron beam produces observable plasma radiation? In addition to the possibility of strong free-free absorption, downward-moving beams may not become unstable at all and thus would not emit coherent radio waves. A bump on the tail of the down-going electron distribution may not develop, and the instability is not driven (*a*) if the distance from the acceleration site to the transition region is too small, and (*b*) if the acceleration process continuously feeds electrons into the same flux tubes, thereby preventing the formation of a bump-on-tail distribution. Sensitive single frequency measurements at 1.6 GHz have shown a surprisingly good correlation of downward-drifting type III bursts and HXR (Sawant et al 1990), suggesting that the problem may also be one of radio sensitivity.

One-to-one correlations between down-going type III bursts and HXR peaks were studied by Aschwanden et al (1993), who used spectrometer data in the 0.1–3 GHz range. They found the HXR peak of 25- to 100-keV HXRs generally occurs before the end of the type III burst. This is consistent with the observed slow drift of the radio bursts. The radio emission seems to originate from electrons with energies of only a few keV.

To summarize, it is now clear that flare electron beams often emit radio waves on their path from the acceleration site down to the chromosphere, where they are then stopped and emit HXRs. The correlation of radio waves from down-going electrons with HXR thick-target emission is well established, although a comprehensive analysis has not yet been done.

RELATION OF TYPE III BURSTS TO SXR STRUCTURES The problem of where type III bursts occur in relation to coronal structures is one of long standing. Type III bursts often appear at heights that are much higher than would be expected on the basis of coronal density models (e.g. Mercier & Rosenberg 1974). Two possible solutions have been considered: (*a*) that propagation effects determine the apparent height of the source; (*b*) that type IIIs preferentially occur in overdense coronal structures.

Numerous statistical studies tend to support the former interpretation of source positions and conclude that type IIIs show no particular preference for overdense structures. For example, Leblanc et al (1974) found that dense streamers do not overlie type III–producing active regions in general. Using stereoscopic observations, Poquerusse et al (1988) concluded that type IIIs occur *between* active regions and dense streamers. Steinberg et al (1984) found that interplanetary type IIIs usually occur in regions of average density.

With the availability of both imaging instruments at dm-λ/m-λ (Nançay Radioheliograph, VLA) and SXRs (*Yohkoh* SXT), there is renewed interest in relating classical radio bursts with coronal structures. There are now many

examples of associations between m-λ type III or type U bursts with SXR structures. Pick et al (1994) showed that a type III/U burst traced out an archlike structure some distance above an SXR-emitting branch. Aurass et al (1994), Kundu et al (1995b), and Raulin et al (1996) have shown associations between SXR jets and type III and/or type U bursts. Kundu et al (1995c) found type IIIs associated with a flaring X-ray bright point. Kundu et al (1995b) and Raulin et al (1996) cited examples of type III/SXR-jet associations as evidence that type IIIs do indeed occur in overdense structures. While type III bursts (or U bursts) and SXR jets may be caused by the same energy release event, given the relatively poor angular resolution of the radio observations and propagation effects, the case for type III bursts preferentially occurring in overdense SXR-emitting structures is not yet compelling. Aurass et al (1994) and Aurass & Klein (1997) showed that electron beams from a given acceleration site can be injected into structures with significantly different magnetic connectivity, which is consistent with past studies (Lantos et al 1984, Pick & Ji 1986).

In summary, recent work on relating electron beams to coronal structures has focused on relating classical burst types to SXR-emitting structures. These have produced several examples of m-λ type U and type III bursts seen in association with weak energy release events—SXR jets and X-ray bright points. However, the question of what path the electron beam follows and to what degree propagation effects determine the apparent source location remains unanswered at present.

THE NATURE OF ELECTRON BEAM ACCELERATION Since each type III burst is the signature of at least one electron beam, radio emission yields information on the acceleration process in time and space. The number of type III bursts in a flare can be as high as several hundred at dm-λ. Some of these bursts stop at lower frequencies, form U bursts, or combine into a smaller number of m-λ bursts. The number of type IIIdm bursts often exceeds the number of HXR peaks, as observed with current instruments, by an order of magnitude. Aschwanden et al (1990) have presented a flare in which there was a close correlation between the type III burst rate at ∼300 MHz and the HXR flux. This correlation suggests a sequence of acceleration events of similar energy, each producing a type III burst and a constant HXR fluence. The large number of required electron beams has been used as an argument for "fragmentation" of the flare energy release (Benz & Aschwanden 1992; see below).

It is a long-standing, hotly debated question whether there is any order in the timing of type III bursts. In single frequency measurements and in spectrograms, there often appears to be a periodicity of the major bursts (Mangeney & Pick 1989), although peaks in the Fourier spectrum are rare and questionable. More refined analyses of groups of type IIIs characterize their recurrence as

quasiperiodic (Aschwanden et al 1994). An analysis of 13 events by Isliker & Benz (1994b) did not yield any low-dimensional correlation dimension. This excludes simple accelerator that can be described with less than 4–6 variables, such as the superposition of a few eigen oscillations. The acceleration process producing individual type III bursts must either be part of a system with more degrees of freedom or be produced stochastically. The apparent quasiperiodicity may be interpreted in terms of the "red noise" character of the type III burst timing (Isliker 1996).

In summary, the time structure of type IIIdm bursts strongly suggests that energy release and acceleration processes are much more fragmented in nature than the HXR observations suggest. Simple accelerator physics is excluded; the acceleration process (or processes) apparently involves more than 4–6 degrees of freedom or is stochastic in nature.

SIGNATURES OF EVAPORATION IN TYPE IIIDM BURSTS? When beams propagate to the chromosphere and lose their energy through collisions, the chromospheric plasma is heated more rapidly than it can radiate the energy away. It therefore responds dynamically, expanding mostly along the magnetic field lines. The dense, hot material is expected to move up as a shock (e.g. Fisher 1987), hitting the upstream plasma. The upward motion of the heated plasme is known by the misnomer of chromospheric evaporation. It has been observationally established from the line broadening and blueshifts in SXR lines of Ca XIX and Fe XXV (e.g. Antonucci et al 1982, Doschek et al 1986) and by direct SXR imaging. The observations suggest that evaporation fills up a large volume with a density of $\sim 10^{11}$ cm^{-3}.

Aschwanden & Benz (1995) have modeled the consequences for radio emission of downward-moving beams, penetrating the evaporation front. They found that the plasma behind the shock front becomes more transparent to plasma emission owing to its higher temperature and the vertical density gradient. The favorable conditions disappear behind the contact surface. The evaporation front creates a moving window for plasma emission that increases in height with time and thus opens to decreasing frequencies.

Indeed, fast-drifting radio emissions are observed frequently in 0.3- to 3-GHz spectrograms with expected characteristics (Aschwanden & Benz 1995). The groups of type III–like bursts have sharp high-frequency cutoffs and similar low-frequency ends. The inferred average drift velocity of the cutoff agent is 240 km/s. It reaches up to 360 km/s. The groups last up to several minutes, and their starts are delayed by about 100 s relative to the start of the associated HXR event. As the density gradients are much steeper than in hydrostatic equilibrium, the drift rates are much higher, which is consistent with the observations. We note, however, that this interpretation is speculative at this point and is in urgent

need of confirmation by simultaneous Doppler shift measurements in SXR spectral lines (e.g. Ca XIX).

A GLOBAL VIEW OF RADIO EMISSION FROM ELECTRON BEAMS The current understanding of the radio emission of electron beams thus leads us to distinguish between two types of coherent beam radiation.

1. "Metric type III bursts" start between 200 and 1000 MHz and generally move upward in the corona. At decreasing frequencies, the bursts of one group overlap in time and combine into one event. Some of them continue to km-λ and thus into the IPM. Many of these m-λ type III bursts are not associated with HXR events. They appear to be a phenomenon of the high corona and seem to have easy access to open field lines. Reversed drift type III bursts and U bursts below 200 MHz are rare.

2. "Decimetric type III bursts," or type IIIdm bursts, occur most commonly in the 400- to 800-MHz range but can occur at lower (200 MHz) and much higher frequencies. They are clearly more numerous than m-λ bursts. Drifts in both directions are observed, and high time-resolution spectrograms often reveal U bursts. Type III bursts above 1 GHz generally have downward motion in the corona. The changeover from upward- and downward-moving beams is usually in the band from 0.4 to 1 GHz. The demarcation is often not well defined in a particular event, indicating a scatter of the density in the acceleration regions between 10^9 and 10^{10} cm^{-3}. Some cases, however, have been reported where the demarcation is at a definite frequency, from where bidirectional beams seem to originate (Aschwanden et al 1993). In these cases, at least some of the upward-moving type III bursts seemed to be of the m-λ type observable to less than 30 MHz. Type IIIdm bursts are generally associated with electron beams in closed loops of active regions.

Figure 9 summarizes the above observational results in a cartoon and puts them into the framework of the cusp model of reconnection. Energy release is assumed to occur in the low corona in a highly fragmented manner via fast magnetic reconnection (see Section 6.1), producing a multitude of bidirectional electron beams. Upward-directed beams that gain access to open field lines produce m-λ type III bursts; those which remain in close magnetic structures produce a type U burst. Downward-directed electron beams produce reverse-slope type IIIdm bursts. The reverse-slope type IIIdm bursts may be modified in time as chromospheric evaporation proceeds. Clearly, the cartoon cannot do justice to all flares.

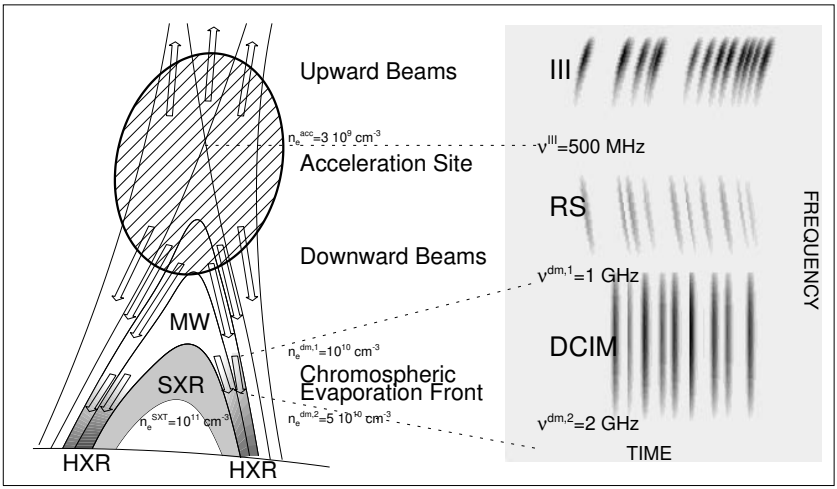

Figure 9 Cartoon of a flare model suggesting a global view of acceleration and evaporation processes in the context of density measurements by coherent radio bursts and SXR emission. The *panel* on the *right* illustrates a radio spectrogram (dynamic spectrum) with bursts indicated schematically. The acceleration site is located in a low-density cusp from where electron beams are accelerated in upward (m-λ type III and type U bursts) and downward (reverse-slope or RS type IIIdm bursts) directions. Downward-precipitating beams that intercept the chromospheric evaporation front may show as decimetric bursts (DCIM) with almost infinite drift rate in the 1- to 2-GHz range. The chromospheric upflow fills SXR-bright loops with subsequently wider footpoint separation while the reconnection point rises higher. (From Aschwanden & Benz 1997.)

4.3 *Narrowband Spikes*

A second class of coherent radio emissions deserves attention, as it is closely associated in time with flare particle acceleration and has the potential to shed some light on the unknown processes involved with energy release. These are the short ($\leq$0.1 s) and narrowband ($\Delta\nu/\nu \leq$ few percent) emissions of dm-λ and m-λ spikes. Dm-λ and m-λ spike bursts are associated with flares and m-λ type III bursts, respectively.

Discovered in the early 1960s around 300 MHz, narrowband spikes were at first the concern of only a small group of observers, who were perplexed by their extremely short duration. This changed when Dröge (1977) and Slottje (1978) discovered them also at 1.4 and 2.8 GHz, respectively, during the rise phase of flare-associated gyrosynchrotron emission. Early spike observations have been reviewed by Benz (1986). Models involving electron cyclotron maser emission and other loss-cone instabilities were proposed and elaborated by a wide community of theoreticians (Section 2.2). Narrowband spikes may imply

fragmentation of the energy release in flares yet another order of magnitude higher than type III bursts (Benz 1985). While this "flare fragmentation hypothesis" (see Section 6.1) has not yet been firmly established, the fascinating possibility of a close connection between spikes and acceleration has driven much of the recent spike research.

Although they may originate from the same physical process, it has been useful to classify spikes into two types.

1. At dm-λ and up to 8 GHz, clusters containing up to 10^4 spikes are observed. Dm-λ spikes occur during the impulsive phase of flares and are usually associated with HXR emission (Benz & Kane 1986). They have the highest association rate with flares (95%) of all coherent radio emissions (Güdel et al 1991). However, it is largely a one-way correlation: Only 2% of all HXR events are associated with spikes. The correlation of the frequency-integrated spike flux with HXR is often very close, but the spike activity is delayed relative to impulsive HXRs at 25 keV by 2–5 sec (Aschwanden & Güdel 1992), suggesting that dm-λ spikes are caused by magnetically reflected or trapped electrons having a loss-cone distribution in velocity space (Section 2.1). If this is the case, dm-λ spikes occur far from the acceleration region, near the footpoints of loops. Thus spikes would be another signature of electron propagation.

2. The other type of spike is confined to a narrow frequency range from about 200 to 400 MHz. These "metric spikes" (Figure 10) are closely associated with m-λ type III bursts moving upward in the corona along open field lines. Compared with their high-frequency cousins, m-λ spikes are more than an order of magnitude more frequent. About 30% of the metric type III bursts have associated m-λ spikes (Benz et al 1996a). Often no Hα flare and/or HXR emission is associated with m-λ spikes. Cross-correlations have shown that the average delay between small groups of m-λ spikes and single type III bursts is 30 ± 40 ms if the drift of the type III bursts is extrapolated to the spike frequency (Benz et al 1996a). The coincidence is not consistent with magnetic reflection in a distant footpoint but rather suggests that the spike source is close to, or in, the acceleration site.

CHARACTERISTICS OF NARROWBAND SPIKES The observational characteristics of narrowband spikes are substantially different from type III bursts. First, the instantaneous bandwidth of spikes is more than an order of magnitude smaller than that of type IIIs. The narrow bandwidths suggest the source emits at a natural frequency of the plasma: ν_{Be}, ν_{pe}, or the upper hybrid frequency ν_{UH}. However, since the source is located in the inhomogeneous corona, the characteristic spike frequencies are distributed over a large range. The bandwidth of

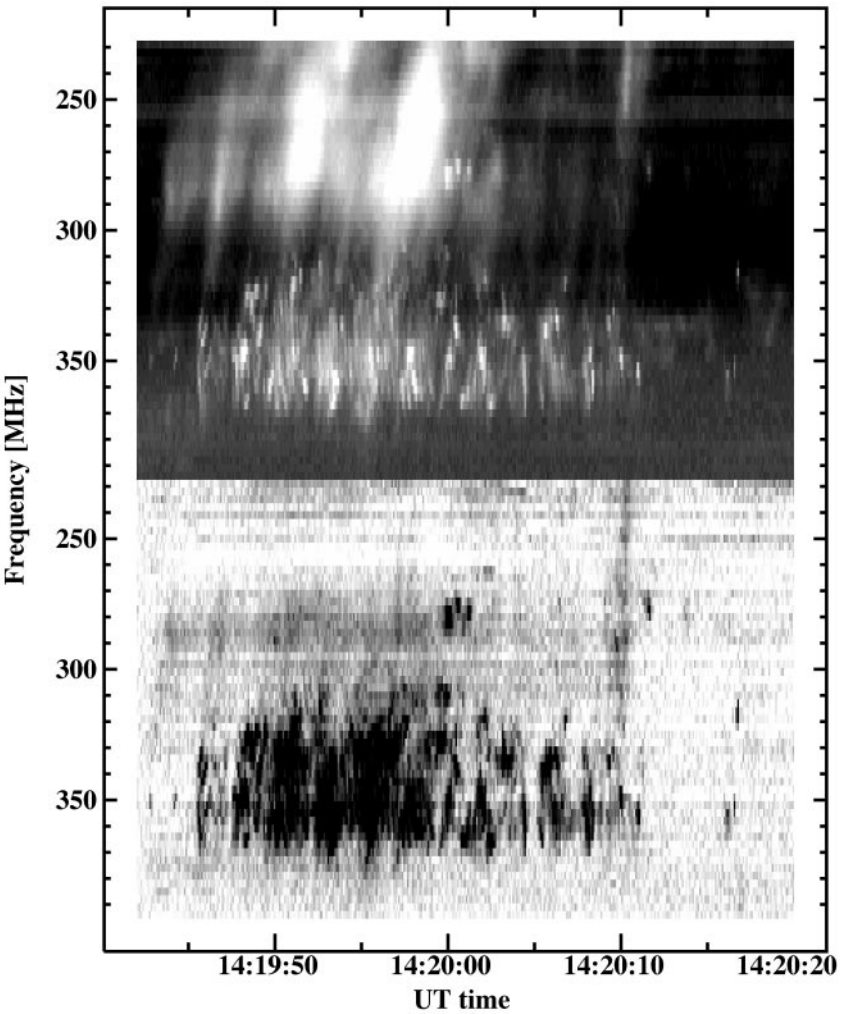

Figure 10 Spectrogram of metric spikes (above 325 MHz) and type III bursts (below 325 MHz) observed on January 1, 1981, by the Ikarus spectrometer near Zurich (Switzerland). *Top*: Enhanced total flux density is shown *bright*. *Bottom*: Degree of polarization, LCP is *dark*. (From Benz et al 1996a.)

an individual spike, $\Delta\nu$, limits the source dimension, L, along the direction of the gradients in either the density or the magnetic field, to (within a factor of 2) $L \lesssim \Delta\nu\Lambda/\nu$, where Λ is the magnetic or density scale. For $\Lambda \approx 10^9$ cm, a typical value in active regions for either case, the source dimension is smaller than 200 km. The observed flux densities (typically $\sim$100 sfu) and the small source sizes imply a brightness temperature in excess of 10^{13} K, indicating coherent emission.

Second, the average spike duration is a factor of 10 shorter than the duration of type III bursts. The decay of single spikes can be fitted by an exponential in time. The decay time decreases inversely with frequency and is surprisingly close to the thermal collision time, assuming a temperature of 3×10^6 K and a density given by $\nu_{pe} \approx \nu$ (Güdel & Benz 1990).

Third, in contrast to type IIIs, the degree of circular polarization is generally high for spikes occurring near the center of the disk, where propagation effects are less severe (Güdel & Zlobec 1991). The sense of polarization, an important diagnostic for the radiation process, is still controversial. Güdel & Zlobec found that dm-λ spikes are polarized in the sense of the x-mode in relation to the leading spot of the associated active region and to associated type III bursts. Benz & Pianezzi (1997), however, found the weaker mode of dm-λ spikes delayed by a fraction of a millisecond, indicating polarization in o-mode during most of the propagation near the Sun. The solution of this enigma may be in the global structure of the coronal magnetic field of the active region. It can not only change direction from the leading spot to the source region, but it also can invert the mode of the radio emission in a quasitransverse region (Section 2.2).

The ordering of spikes in the frequency-time domain has received considerable interest as a possible diagnostic for the acceleration process. There is general agreement that there is no order in time at a given frequency (e.g. Isliker & Benz 1994b). As noted above, the bandwidth reflects the source dimension. The bandwidth of spikes shows a wide distribution with a decreasing slope to wider bandwidths (Csillaghy & Benz 1993). In a preliminary study of two cases by Karlicky et al (1996), the frequency distribution of scales is a power-law with a slope close to 5/3, resembling that of a Kolmogorov spectrum of cascading turbulent waves.

M-λ spikes are confined to a small range of frequencies, and sometimes several harmonics are observed. A correlation study by Krucker & Benz (1994) has revealed a preference for harmonic ratios of 2.5:3.5. The modulation of the harmonics correlates in time, indicating a common source for individual spikes at harmonic frequencies. Willes & Robinson (1996) have shown that the noninteger harmonic structure of m-λ spikes may be explained by a variant of the cyclotron maser mechanism, where Bernstein waves are unstable to growth

by the cyclotron maser instability. The Bernstein waves then coalesce to form a transverse wave ($B + B' \Rightarrow T$) that escapes from the source.

5. QUASISTEADY ENERGY RELEASE AND CORONAL HEATING

Energy release must occur in the Sun's atmosphere on a more or less continuous basis, as required by the existence of the corona and solar wind. Parker (1988) suggested that "nanoflares," transient flare-like events involving $\sim 10^{24}$ ergs or less, may heat X-ray–emitting coronal loops. Hudson (1991) has considered the question of whether the smallest energy releases were likely to play a significant role in heating the corona. He pointed out that because the flare frequency distribution function is a power law characterized by an index $\alpha < 2$ for event energies in the range of $\lesssim 10^{27}$ ergs up to the largest flares, the total power in the distribution is dominated by the events with the largest energies—hence the *observed* flare frequency distribution contains insufficient energy to heat the corona. In order for nanoflares to contribute significantly to coronal heating, the flare frequency distribution must possess a soft component ($\alpha > 2$) at small event energies.

Radio observations are by far the most sensitive means of detecting very weak, nonthermal, flare-like events. The weakest nonthermal HXR events observed to date are those reported by Lin et al (1984), who observed nonthermal HXR "microflares" with energies of $\gtrsim 10^{26}$ ergs. As we now show, radio observations probe nonthermal, flare-like events with energies of 10^{25} ergs in their incoherent radio emission. Energy release events with energies $\ll 10^{24}$ ergs may be seen in coherent emission. Nonthermal HXR emission is undetectable from such events with the current and future generation of HXR instruments (HXT, BATSE, HESSI).

5.1 *Transient Energy Release in Active Regions*

The best-known radio signatures of sporadic or quasisteady energy release in and above solar active regions are type III (Section 4 and Section 5.3) and type I radio bursts (Kai et al 1985), respectively. Mercier & Trottet (1996) presented an analysis of type I storms that may point toward a significant steepening of the frequency distribution function of energy release events at extremely small energies. They form the frequency distribution as a function of peak flux density of type I bursts and find that it is steep ($\alpha \approx 3.0$). Similar results were obtained at different frequencies (164, 237, and 327 MHz) and even in different active regions. Model calculations suggest that as little as 10^{21} ergs are needed for a single type I burst. Hence, type I bursts may represent the smallest discrete releases of energy observable. However, in view of the

fact that the emission mechanism of type I bursts is not fully understood, one must be cautious about interpreting the frequency distribution of type I bursts as a function of the underlying energy released.

At shorter wavelengths, persistent microburst activity is seen in active regions at both dm-λ (Bastian 1991) and cm-λ (Gopalswamy et al 1994, Shibasaki 1996), although the two likely involve different emission mechanisms. Shimizu et al (1992) drew attention to the phenomenon of SXR transient brightenings in active regions, first imaged by the SXT on *Yohkoh*. White et al (1995) examined radio counterparts to a sample of active region SXR transients at 17 GHz and concluded that there is little evidence for the presence of nonthermal electrons in these events. However, Gary et al (1997) noted that somewhat lower frequencies are more sensitive to nonthermal electrons. Comparing broadband spectroscopic observations at cm-λ (obtained with the OVRO Solar Array) with observations of 34 SXR transients (obtained by the SXT) (Figure 11), they found that most SXR transients ($\approx$85%) have a detectable cm-λ counterpart and that many show evidence for the presence of nonthermal electrons. On this basis, Gary et al concluded that the active region transient brightenings are indeed tiny flares and may be regarded as the low energy extension (to $\sim 10^{26}$ ergs) of the flare distribution function. Shimizu (1995) found that their distribution as a function of energy is a power law with an index of 1.5–1.6 and concluded that active region SXR transients are unable to heat active region loops, falling short by a factor of $\sim$5.

5.2 *Transient Energy Release in Quiet Regions*

In quiet regions, Krucker et al (1997a) have identified small radio and SXR transients in the chromospheric network using the VLA at 15 GHz and deep exposures with the SXT. These "network flares" occur on the solar disk at a rate of about one every 3 s, have a duration of $\sim$10 min, and release a few times 10^{25} erg, roughly an order of magnitude smaller than the minimum detectable energies of active region SXR transients. Krucker et al (1997a) pointed out the high polarization of some radio events and the possibility that they are due to gyrosynchrotron emission. They estimated that energy deposition by network flares falls short of that needed to heat the quiet corona by more than an order of magnitude, although the uncertainties are large.

It is noteworthy that, using the observed relation of $\approx$12.5 counts/s in HXRs (>30 keV) for 1 sfu in gyrosynchrotron emission at 17 GHz (Kosugi et al 1988), the HXRBS detector on SMM would have seen 0.018 counts/s at peak flux for the miniflare shown in Figure 12, well beyond the capabilities of current or planned (e.g. HESSI) HXR detectors. Radio observations are currently the only way to detect nonthermal particles and to investigate the flare character of such brightenings.

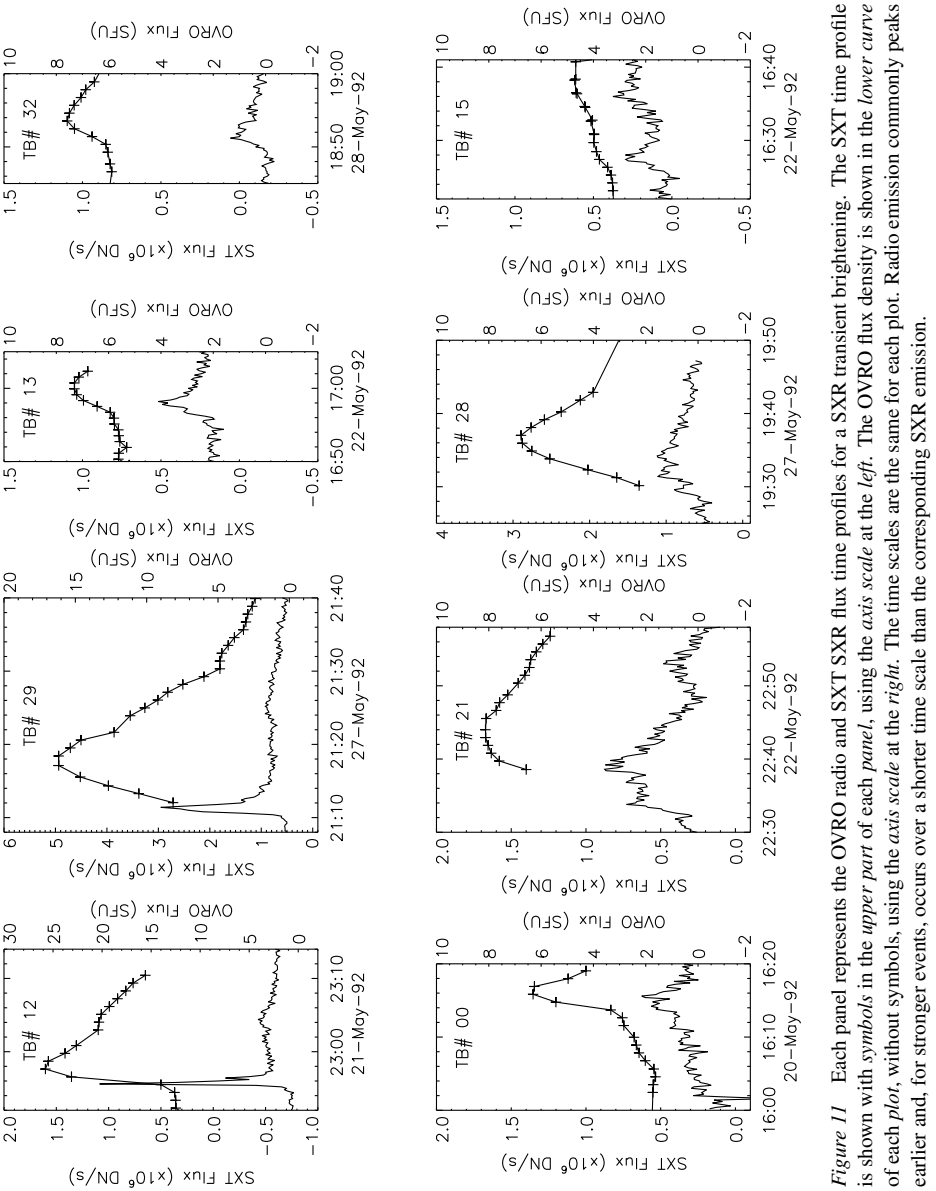

Figure 11 Each panel represents the OVRO radio and SXT SXR flux time profiles for a SXR transient brightening. The SXT time profile is shown with *symbols* in the *upper part* of each *panel*, using the *axis scale* at the *left*. The OVRO flux density is shown in the *lower curve* of each *plot*, without symbols, using the *axis scale* at the *right*. The time scales are the same for each plot. Radio emission commonly peaks earlier and, for stronger events, occurs over a shorter time scale than the corresponding SXR emission.

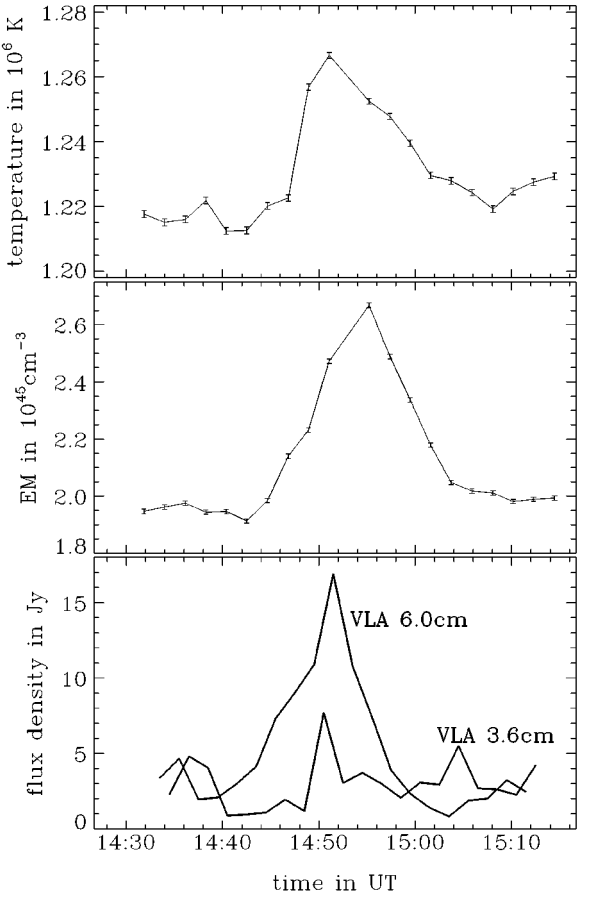

Figure 12 The time profiles of a tiny flare-like transient in the network of a quiet region of the Sun. *Top*: Average temperature over the area of coronal extreme ultraviolet intensity as derived from SOHO/EIT observations; no background was subtracted. *Middle*: Total emission measure of the flare area at temperatures above 10^6 K. *Bottom*: Radio flux density observed simultaneously by the VLA at 6- and 3.6-cm wavelengths. The 3-cm emission does not show a significant peak. (From Krucker et al 1997b.)

5.3 *Type III Bursts in the Upper Corona*

In Section 4.2, we note that weak type IIIs occurring high in the corona correlate most poorly with HXR bursts. Yet they represent discrete episodes of energy release in the upper corona and occur whenever active regions are present. The tiniest type III bursts were identified in the upper corona at 38 and 74 MHz ($\lambda \sim 4$ and 8 m) by the CLRO (Kundu et al 1986, White et al 1987). Kundu et al suggested that they involve several orders of magnitude less energy than

conventional type III bursts; i.e. far less than $\sim 10^{25}$ ergs. It is worth asking what the relationship of these tiny type III–like events is to the "super-halo" component of electrons in the IPM discussed by Lin (1997). The 3D Plasma and Energetic Particle experiment on board the WIND spacecraft has discovered a super-halo electron population in the IPM during periods free from solar energetic particle events and streams. This quiet-time super-halo is a nonthermal population of electrons with energies ~2–100 keV, believed to be of solar origin. Some energy release process in the upper corona must accelerate the super-halo component on a nearly continuous basis during quiet times.

In summary, transient energy releases involving 10^{26} ergs down to a few times 10^{24} ergs have been detected using radio techniques. At energies $\gtrsim 10^{25}$ ergs, these events are often found to be the radio counterparts of SXR transients (e.g. active region transients and network flares). However, the active region SXR/radio transients do not play a dominant role in heating active region loops, and network flares do not appear to contribute significantly to the energy budget of the quiet corona. Work on the smallest energy releases—type I bursts and weak type III bursts, possibly with energies $\ll 10^{24}$ ergs—is suggestive, but their role in the energy budget of the corona and solar wind has not yet been established.

6. WHAT DO RADIO OBSERVATIONS TELL US ABOUT FLARES?

Previous sections have organized recent work on flares according to the physics of the underlying emission mechanisms—primarily gyrosynchrotron emission or plasma radiation—and their relation to high-energy photon emissions from energetic electrons. We now wish to place the radio observations described in these sections in a broader interpretive context and, in so doing, return to the questions raised in the Introduction. We also point out ways in which radio observations can lead to further progress on these issues.

6.1 *Energy Release*

SITE OF ENERGY RELEASE The site of energy release in flares is the low corona. At radio wavelengths, there are at least two lines of evidence. At dm-λ, the existence of downward-directed electron beams suggests electron energization and injection in the corona (Section 4.2). The existence of bidirectional electron beams allows the identification of the frequency, and hence density, that demarcates upward-directed and downward-directed electron beams. The densities inferred in the beam acceleration sites is significantly smaller than that in the underlying SXR loops. Aschwanden & Benz (1997) found $n_{acc} = (0.6\text{–}10) \times 10^9$ cm^{-3} and $n_{SXR} = (0.2\text{ –}2) \times 10^{11}$ cm^{-3}, again implying energy release above the SXR-emitting loops. These results are illustrated schematically in Figure 9.

To make further progress, imaging spectroscopy at dm-λ is needed to determine precisely where bidirectional beams occur within a flaring active region. While scattering may prove to be a limitation for frequencies below 1–2 GHz, the fact that type IIIdm bursts occur at frequencies of several GHz may enable spectroscopic imaging observations to pinpoint the origin of electron beams in flaring active regions, and hence the energy release site, to a few arcsec.

MEANS OF ENERGY RELEASE Fast magnetic reconnection is now widely accepted as the most plausible means of energy release in flares. Cusp morphologies, arising in coronal magnetic arcades, have received a great deal of recent attention. Here magnetic reconnection proceeds from lesser to greater heights. With the discovery of HXR sources over SXR loop tops (Masuda et al 1994), cusp morphologies have been proposed as a "universal" magnetic configuration for both LDE and impulsive flares (e.g. Shibata et al 1995, Tsuneta et al 1997). Morphological studies at cm-λ (Section 3.3) indicate that loop-loop interactions also play an important role in producing impulsive flares. Insofar as both morphologies appear to be favorable to fast magnetic reconnection, there may be no fundamental difference between the two cases.

Magnetic reconnection in two dimensions is now fairly well understood (Priest & Forbes 1986, Priest 1991), but no quantitative models for magnetic reconnection in three dimensions yet exist. Melrose (1995) has emphasized the need to consider reconnection within a global model that includes both the magnetic field and large-scale current systems. One recent approach to understanding the 3D magnetic field topology is to attribute the coronal magnetic field to a distribution of photospheric point charges, the so-called magnetic charge topology (MCT) models (Longcope 1996 and references therein). MCT models are inherently current free. Longcope has extended the MCT model to admit currents ["minimum current corona" (MCC) models], providing a means of estimating the energy stored in particular magnetic topologies as well as changes in magnetic connectivity due to flaring.

Most of the work done on the 3D magnetic topology in flaring active regions has been done by mapping Hα kernals in relation to topological structures, although ultraviolet and X-ray data have also been used (see Bagalá et al 1995 and references therein). Evidence for changing magnetic connectivity in radio and X-ray images has been purely qualitative. SXR images from *Skylab* (e.g. Kahler 1977) and, more recently, the SXT (Sakurai et al 1992) reveal changes in the magnetic field configuration from before to after a flare that suggest a change from a nonpotential to a more nearly potential magnetic field configuration. Such results are ambiguous, however, owing to uncertainty in whether the same magnetic field lines are being traced out by thermal plasma before or after the flare. Similarly, maps made by the VLA (Kundu et al 1982, Willson 1983,

Shevgaonkar & Kundu 1985) and the Nobeyama radioheliograph (Hanaoka 1996, 1997, Nishio et al 1997) have been interpreted in terms of interacting magnetic loops, or loop systems, particularly within the context of magnetic flux emerging into preexisting magnetic structures.

Radio imaging observations (e.g. Figure 4) are potentially more robust tracers of changing connectivity of the magnetic field as the flare progresses. Unlike SXR observations, radio imaging observations trace out the volume instantaneously accessible to nonthermal electrons. Full exploitation of cm-λ observations requires imaging at many frequencies in order to reveal complex loop structures in their entirety (Section 3.2). This aspect of radio imaging observations has not yet been exploited but holds promise for detailed comparisons with MCT/MCC or similar model formulations.

THE NATURE OF ENERGY RELEASE The term flare fragmentation refers to the possibility that energy release and/or particle acceleration involves a multitude of discrete events. The idea of flare fragmentation is not a new one; it dates back more than two decades (see Bastian & Vlahos 1997 for a review). Current interest in the flare fragmentation issue is not concerned so much with whether energy release is fragmentary in nature but with how fragmented energy release occurs.

Considerable effort has been directed toward the question of whether energy release is a stochastic process or whether it has any underlying order (Section 4). One of the earliest attempts to account for the flare frequency distribution function was that of Rosner & Vaiana (1978) with what is essentially a "stochastic relaxation" model. Litvinenko (1994) has attempted to place the stochastic relaxation model on a more physical footing by dissipating energy in reconnecting current sheets (RCS). An alternative class of models is one in which discrete episodes of energy release are coupled and fragmentation of the energy release plays an overriding role. An example is the avalanche model for energy release in flares proposed by Lu & Hamilton (1991). Here, the active region is described in terms of a system in a state of "self-organized criticality," an idea explored further using cellular automaton models by Lu et al (1993) and Vlahos et al (1995). More recently, Litvinenko (1996) has incorporated elements of both avalanche and RCS models into a single model in which multiple RCS interact during flares through coalescence. Interestingly, he is able to reproduce the flare frequency distribution function; furthermore, he finds a soft component in the frequency distribution that is suggestive of an energetically significant population of extremely small energy releases: nanoflares (cf Section 5).

To date, observations have established the fragmentary nature of energy release through structure in the temporal and (radio) frequency domains. Such

fragmentation implies spatial fragmentation as well. While type III and type IIIdm bursts have been imaged at fixed frequencies (Section 4.2), they have not been imaged with the appropriate combination of temporal resolution ($<$1 sec), bandwidth ($\Delta\nu/\nu \sim 1$), frequency ($\nu \sim$ 2–3 GHz to minimize scattering), frequency resolution (1%), and spatial resolution (few arcsec). Such observations will be critical in observing fragmentary energy release.

6.2 *Electron Energization and Acceleration*

Energetic electrons are responsible for the incoherent gyrosynchrotron radiation emitted during flares and for the plasma radiation emitted by type III and type III–like bursts, and they are widely believed to be responsible for the HXR burst as well. A significant fraction of the energy dissipated in a flare is carried by such electrons (Duijveman et al 1982), placing well-known demands on acceleration mechanisms (e.g. Brown 1975), i.e. the acceleration of $\sim 10^{38}$ electrons to energies $>$20 keV on a time scale $\lesssim 10^2$ sec. Simnett (1995) has argued that these demands may be greatly alleviated if protons, not electrons, are the most important energetic particle constituent in flares (although see Brown 1991) and that electrons are a secondary population. That energetic protons play a role in flares is not in dispute—direct evidence in the form of γ-ray lines has been reviewed by Ramaty & Murphy (1987). Furthermore, protons are not only accelerated in a second-phase process, as believed some time ago (Section 1), but are commonly accelerated to high energies in near coincidence with HXR- and radio-emitting electrons. Miller et al (1997) point out that, based on a study by Ramaty et al (1995), the rate at which protons are energized above 1 MeV during impulsive flares rivals that at which electron energization occurs and that there is rough equipartition in the energies of the electron and ion populations for those flares detected in γ-rays. Whether this statement applies to all flares is unknown.

Hence, while the energy content in protons is comparable to that in electrons for some flares, the problem remains: How is a significant fraction of the energy dissipated in a flare transferred to electrons with energies of tens to hundreds of keV? How are some electrons accelerated to energies $>$1 MeV? Recent reviews of work on this issue include those of Melrose (1990), Mandzhavidze & Ramaty (1993), and Miller et al (1997).

ACCELERATION IN RECONNECTING CURRENT SHEETS Electron acceleration presumably occurs during energy release in electric fields induced by the changing magnetic field as part of the magnetic reconnection process. The number of electrons accelerated in this way, and the resulting energy distribution, is unknown. The most tantalizing radio diagnostic of energy release in reconnecting

current sheets is bidirectional electron beams, which manifest themselves as type III–like bursts with a component that drifts downward and another that drifts upward in frequency with time (Section 4.2). Spatially resolved observations of bidirectional beam emission will constrain the source density and its location in time and space, as well as the time evolution of both.

While fast magnetic reconnection may proceed in a localized and fragmentary fashion, it may induce large-scale electric fields, excite a broadband spectrum of waves, or both over spatial scales much larger than the reconnection volume. Electron acceleration via electron runaway and stochastic acceleration have both received recent attention—we touch on both.

ACCELERATION OF RUNAWAY ELECTRONS Electron acceleration to energies $\sim$100 keV is possible via electron runaway down a net potential drop. Two types of electron heating and runaway acceleration have been considered: by large-scale quasistatic electric fields and by multiple weak double layers (WDLs). The former has received far more attention.

In the presence of a DC electric field, an electron experiences the Coulomb force of the electric field and a drag force that increases with electron speed until the electron speed is comparable to v_{te}, beyond which the drag force drops precipitously. The electric field strength where the drag force and the electric field force match when the electron is moving at v_{te} is called the Dreicer field (Dreicer 1960). When the electric field exceeds the Dreicer field (a super-Dreicer field) the entire electron distribution will be freely accelerated, i.e. it will "run away." If the electric field is sub-Dreicer, some part of the distribution may be runaway. The idea of electron runaway acceleration in super- or sub-Dreicer electric fields has been applied frequently to electron acceleration in flares (e.g. Holman 1985, Tsuneta 1985, Holman et al 1989). To avoid a large self-induction magnetic field, the current must filament into many ($\gtrsim 10^4$) oppositely directed current channels.

A runaway distribution of electrons may also be accelerated by interactions with multiple short-lived weak double layers (WDLs; Khan 1989, Melrose 1990). The current running along a magnetic flux tube again filaments into many current channels. Many WDLs form along each current filament, which may then accelerate a runaway distribution of electrons in a series of discrete acceleration events.

Benka & Holman (1992, 1994) have considered DC electric fields as a means of explaining either cm-λ or HXR observations. DC fields are assumed to produce heating (via Joule dissipation) and particle acceleration (via electron runaway), thus producing the thermal/nonthermal (TNT) electron energy distribution alluded to in Section 3.4. However, the problem of accounting for

both HXR and cm-λ observations within the context of DC electric fields in a self-consistent fashion has not yet been addressed and represents an important challenge.

To date, spatially unresolved cm-λ and HXR spectra have been used as observational inputs. Both quasistatic fields and WDLs require an extended spatial region to accelerate electrons. There is a critical need to constrain the electron energy distribution as a function of both space and time in a flaring source. Spatially and temporally resolved cm-λ spectra would provide a diagnostic everywhere in the source that nonthermal electrons are present.

STOCHASTIC ACCELERATION Acceleration by quasistatic electric fields or by WDLs cannot accelerate electrons to energies greater than a few times 100 keV. Other mechanisms must operate to accelerate electrons to high energies in addition to, or instead of, DC electric fields or WDLs. When a turbulent spectrum of waves is present in the flaring source, a seed population of mildly energetic particles can be further accelerated to high energies via second-order Fermi acceleration. Many varieties of stochastic acceleration are possible, depending on the type of waves assumed to be present. Langmuir, Alfvén, whistler, magnetosonic, and upper hybrid waves have all been considered (Mandzhavidze & Ramaty 1993, Miller et al 1997, and references therein).

An attractive picture of electron acceleration in impulsive flares is the following (cf Mandzhavidze & Ramaty 1993). Magnetic reconnection bulk-energizes electrons and sets up DC electric fields and/or WDLs, which cause further plasma heating via Joule dissipation and electron acceleration via electron runaway. The field can vary markedly in time as energy release proceeds, thereby causing rapid changes in the number and energy of fast electrons. These are mainly responsible for prompt cm-λ and HXR emission. DC electric fields and/or WDLs also provide a seed population of electrons and ions (Holman 1995) for further acceleration to high energies by stochastic processes (Miller & Ramaty 1987).

Alternatively, Hamilton & Petrosian (1992) have shown that it is possible to accelerate electrons directly out of the thermal distribution to mildly relativistic energies, possibly removing the need for pre-acceleration by DC electric fields or WDLs. Steinacker & Miller (1992) have shown that high-frequency waves can accelerate electrons out of the thermal distribution to relativistic energies. How would such a high-frequency spectrum of waves be created? Miller et al (1996) have suggested that a cascade of magnetohydrodynamic waves (fast mode) might be a feasible candidate, with input on long wavelengths that are due to large-scale magnetic reconnection processes.

Stochastic acceleration models are also very much in need of robust observational inputs. To date, most observational input has been in the form of spatially

unresolved HXR/γ-ray spectra and in situ measurements of energetic electrons and ions in the IPM. Radio data have not been used as an explicit constraint in such models, with the exception of the work by Lee & Gary (1994). Using SMM/HXRBS and cm-λ spectroscopic measurements from OVRO, Lee & Gary account for the differing decay rates of HXR counts and the cm-λ flux for a GOES M3.1 flare by means of electrons accelerated by turbulence (whistler waves), the turbulence itself perhaps the result of DC electric fields.

What kinds of radio measurements would be suitable? Analyses of the kind suggested by Karlicky et al (1996) (Section 4.3) offer the tantalizing prospect of imposing constraints on the turbulent spectrum of waves available in or near the energy release site and on its evolution in time. Spatially and spectrally resolved cm-λ/mm-λ timing studies (Section 3.6) are another observational input channel that should be exploited. Such observations would reveal when and where electrons are accelerated with energies over the range of tens of keV to several MeV.

6.3 *Electron and Energy Transport*

Many of the observable consequences of catastrophic energy release and particle acceleration in flares result from the transport of energetic particles and hot plasma to sites that are distant from the energy release site. This includes chromospheric Hα emission, prompt HXR footpoint emission, gyrosynchrotron emission from coronal magnetic loops, type III bursts in the upper corona and IPM, and particle measurements in the IPM. In coronal magnetic loops, once energetic electrons have been injected, particle transport is dominated by the mirror force resulting from converging magnetic fields (causing particle trapping) and pitch-angle scattering (causing particle precipitation from the trap). Pitch-angle scattering is caused by Coulomb scattering, by wave-particle interactions with a background spectrum of waves, or in some cases by cyclotron maser emission.

TRAPPING AND PRECIPITATION The relative timing of cm-λ and HXR emission is discussed in Section 3.6. The most promising candidate for timing differences is electron trapping or some kind of "second step" or delayed acceleration of electrons. Based on detailed studies of HXR timing between 20–200 keV, Aschwanden et al (1996, 1997) have concluded that fine structures in the HXR emission from impulsive flares can be attributed to energetic electrons that precipitate directly from the magnetic loop. Aschwanden et al (1997) attribute the smoothly varying component of HXR flux variations to the energy-dependent precipitation of a magnetically trapped population of electrons. It is assumed that the precipitation is mediated by Coulomb collisions, which scatter electrons into the loss cone, thereby allowing them to precipitate from the trap.

While electron trapping and precipitation, mediated by Coulomb collisions, seem to account for the observed properties of both rapidly and smoothly varying components of HXR photons with energies $\lesssim$200 keV, Ramaty et al (1994) suggest a different picture for more energetic emissions. On the basis of a study of mm-λ and γ-ray emissions from the series of X-class flares in June 1991, Ramaty et al (1994) concluded that electron trapping was mediated by plasma turbulence, not Coulomb collisions, and that pitch angle scattering by an evolving distribution of turbulence was responsible for the changing ratio of electron bremsstrahlung to gyrosynchrotron radiation with time.

CHROMOSPHERIC EVAPORATION Chromospheric heating by an intense flux of nonthermal electrons causes material to ablate from the chromosphere and to enter the corona, increasing the density of thermal SXR-emitting plasma (Section 4.2). It is suggested that downward-directed type IIIdm bursts can be used as a probe of this process. In Section 3.4, we point out that the steep spectral slopes observed in cm-λ spectra could be explained by Razin suppression by the ambient medium. Enhanced free-free absorption or an increasing plasma cutoff frequency resulting from an increase in the density of the ambient medium can also modify the cm-λ spectrum with time. Finally, multiband imaging observations of mm-λ emission from warm, dense plasma ablated from the chromosphere (Section 3.5) will be a valuable temperature and density diagnostic. All of these tools can be brought to bear on the problem of chromospheric evaporation, which is itself an aspect of electron transport.

7. SUMMARY AND FUTURE PROSPECTS

Radio observations of flares have proceeded along two orthogonal tracks: imaging at fixed frequencies and broadband spectroscopic observations with little or no spatial resolution. Imaging observations at cm-λ and, more recently, mm-λ have clarified the relationship between radio, SXR, and HXR emission, opening the way to exploit joint radio/X-ray observations as a diagnostic of energy release and transport in solar flares. Spectroscopic observations at dm-λ have allowed us to exploit plasma radiation from nonthermal beams of electrons to probe the energy release site and its immediate environment. Spectroscopy at cm-λ has offered insights into accelerator physics and the role of the ambient medium and has given us a glimpse of the considerable diagnostic power of cm-λ spectroscopy. The sensitivity of radio emission to even small numbers of energetic electrons allows the smallest energy releases to be studied in both their incoherent and coherent emissions.

Where do we go from here? In our opinion, the potential of radio diagnostics has barely been tapped. A recurrent theme in Section 6 is the need to

combine imaging with broadband spectroscopy across the dm-λ, cm-λ, and even the mm-λ bands to address the fundamental questions of energy release (site, means, nature), of particle acceleration (DC fields, WDLs, stochastic processes), and of particle transport (magnetic connectivity, trapping, pitch angle scattering, chromospheric ablation). With a solar-dedicated instrument capable of performing high-resolution imaging spectroscopy over the cm-λ and dm-λ bands, an extremely powerful tool that is complementary to X-ray and optical observations would be brought to bear on the fundamental problems discussed above, integrating the many radio diagnostics discussed in this review into a comprehensive view of the flare phenomenon. Such an instrument does not yet exist and must be a goal for the solar community.

ACKNOWLEDGMENTS

We thank our colleagues GA Dulk, M Güdel, HS Hudson, and T Kosugi for discussion and comments on an early draft of this review. TSB would like to acknowledge the hospitality of the radioheliograph group at the Nobeyama Radio Observatory, where he stayed as Foreign Research Fellow of the National Astronomical Observatory of Japan while part of this work was done. AOB acknowledges partial support by Swiss National Science Foundation Grant Number 20-46656.96. DEG acknowledges partial support by National Science Foundation Grant ATM-9613832 to the New Jersey Institute of Technology.

Literature Cited

Alissandrakis CE, Nindos A, Kundu MR. 1993. *Sol. Phys.* 147:343–58
Altyntsev AT, Grechnev VV, Kachev LE, Lesovoi SV, Mansyrev MI, et al. 1994. *Astron. Astrophys.* 287:256–60
Antonucci E, Gabriel AH, Willson RF, Slottje C, et al. 1982. *Sol. Phys.* 78:107–23
Arnoldy RL, Kane SR, Winckler JR. 1967. *Sol. Phys.* 2:171–78
Arnoldy RL, Kane SR, Winckler JR. 1968. *Ap. J.* 151:711–36
Aschwanden MJ, Bastian TS, Benz AO, Brosius JW. 1992. *Ap. J.* 391:380–92
Aschwanden MJ, Benz AO. 1995. *Ap. J.* 438: 997–1012
Aschwanden MJ, Benz AO. 1997. *Ap. J.* 480: 825–39
Aschwanden MJ, Benz AO, Dennis BR, Schwartz RA. 1995a. *Ap. J.* 445:347–65
Aschwanden MJ, Benz AO, Montello ML. 1994. *Ap. J.* 431:432–49
Aschwanden MJ, Benz AO, Schwartz RA. 1993. *Ap. J.* 417:790–804
Aschwanden MJ, Bynum RM, Kosugi T, Hudson HS, Schwartz RA. 1997. *Ap. J.* 487:936–55
Aschwanden MJ, Güdel M. 1992. *Ap. J.* 401: 736–53
Aschwanden MJ, Montello ML, Dennis BR, Benz AO. 1995b. *Ap. J.* 440:394-406
Aschwanden MJ, Schwartz RA, Benz AO, Lin RP, Pelling RM. 1990. *Sol. Phys.* 130:39–55
Aschwanden MJ, Wiehl HJ, Benz AO, Kane SR. 1985. *Sol. Phys.* 97:157–72
Aschwanden MJ, Wills MJ, Hudson HH, Kosugi T, Schwartz RA. 1996. *Ap. J.* 468:398–417
Aurass H, Klein K-L. 1997. *Astron. Astrophys. Suppl. Ser.* 123:279–304
Aurass H, Klein K-L, Martens PCH. 1994. *Sol. Phys.* 155:203–6

Baars JWM, Hooghoudt BG. 1973. *Astron. Astrophys.* 31:323–31
Bagalá LG, Mandrini CH, Rovira MG, Démoulin P, Hénoux JC. 1995. *Sol. Phys.* 161:103–21
Bai T, Dennis BR. 1985. *Ap. J.* 292:699–715
Bai T, Ramaty R. 1979. *Ap. J.* 227:1072–81
Bai T, Sturrock PA. 1989. *Annu. Rev. Astron. Astrophys.* 27:421–67
Bastian TS. 1991. *Ap. J. Lett.* 370:L49–52
Bastian TS. 1994. *Ap. J.* 426:774–81
Bastian TS. 1995a. *Infrared Tools for Solar Physics: What's Next?,* Proc. 15th NSO/Sac Peak Workshop, ed. JR Kuhn, MJ Penn, pp. 115–26. Singapore: World Sci.
Bastian TS. 1995b. *Ap. J.* 439:494–98
Bastian TS, Aschwanden MJ. 1998. *Ap. J.* In press
Bastian TS, Gary DE. 1992. *Sol. Phys.* 139:357–85
Bastian TS, Kiplinger A. 1991. In *Max 1991 Workshop #3, Estes Park, CO*, ed. R Winglee, A Kiplinger, pp. 153–71
Bastian TS, Vlahos L. 1997. In *Coronal Physics from Radio and Space Observations, Lect. Notes Phys.*, ed. G Trottet, pp. 68–90. Berlin: Springer-Verlag
Belkora L. 1997. *Ap. J.* 481:532–44
Benka SG, Holman GD. 1992. *Ap. J.* 391:854–64
Benka SG, Holman GD. 1994. *Ap. J.* 435:469–81
Benz AO. 1985. *Sol. Phys.* 96:357–70
Benz AO. 1986. *Sol. Phys.* 104:99–110
Benz AO. 1993. *Plasma Astrophysics: Kinetic Processes in Solar and Stellar Coronae.* Dordrecht: Kluwer. 299 pp.
Benz AO, Aschwanden MJ. 1992. In *Eruptive Solar Flares*, ed. Z Svetska, BV Jackson, ME Machado, IAU Colloq. 133, pp. 106–15. Berlin: Springer-Verlag
Benz AO, Bernold TEX, Dennis BR. 1983. *Ap. J.* 271:355–66
Benz AO, Csillaghy A, Aschwanden MJ. 1996a. *Astron. Astrophys.* 309:291–300
Benz AO, Fürst E, Hirth W, Perrenoud MR. 1981. *Nature* 291:210–11
Benz AO, Graham D, Isliker H, Andersson C, Koehnlein W, et al. 1996b. *Astron. Astrophys.* 305:970–76
Benz AO, Güdel M, Isliker H, Miszkowicz S, Stehling W. 1991. *Sol. Phys.* 133:385–93
Benz AO, Kane SR. 1986. *Sol. Phys.* 104:179–85
Benz AO, Magun A, Stehling W, Su H. 1992. *Sol. Phys.* 141:335–46
Benz AO, Pianezzi P. 1997. *Astron. Astrophys.* 323:250–58
Bogod VM, Korzhavin AN, Akhmedov SHB, Aurass H, Hildebrandt J. 1990. *Sol. Phys.* 129:351–61
Brown JC. 1975. In *Solar Gamma-, X-, and EUV Radiation*, ed. S Kane, IAU Symp. 68, pp. 245–82. Dordrecht: Reidel
Brown JC. 1991. *Philos. Trans. R. Soc. London Ser. A* 336:413–24
Cairns IV, Robinson PA. 1995. *Ap. J.* 453:959–72
Cane HV. 1984. *Astron. Astrophys.* 140:205–9
Chertok IM, Fomichev VV, Gorgutsa RV, Hildebrandt J, Krüger A, et al. 1995. *Sol. Phys.* 160:181–98
Cliver EW. 1996. In *High Energy Solar Physics*, ed. R Ramaty, N Mandzhavidze, X-M Hua, pp. 45–60. New York: Am. Inst. Phys.
Cliver EW, McNamara LF, Gentile LC. 1985. *J. Geophys. Res.* 90:6251–66
Cohen M. 1960. *Ap. J.* 131:664–80
Cornell ME, Hurford GJ, Kiplinger AL, Dennis BR. 1984. *Ap. J.* 279:875–81
Correia E, Kaufmann P, Magun A. 1994. In *Infrared Solar Physics*, ed. DM Rabin, JT Jeffries, C Lindsey, IAU Symp. 154, pp. 125–29. Dordrecht: Kluwer
Crannell CJ, Frost KJ, Saba JL, Mätzler C, Ohki K. 1978. *Ap. J.* 223:620–27
Csillaghy A, Benz AO. 1993. *Astron. Astrophys.* 274:487–96
Dennis BR. 1988. *Sol. Phys.* 118:49–94
Doschek GA, Antiochos SK, Antonucci E, Cheng C-C, Culhane JL, et al. 1986. In *Energetic Phenomena on the Sun*, ed. MR Kundu, B Woodgate, NASA Conf. Pub. 2439, 4:1–40
Dreicer H. 1960. *Phys. Rev.* 117:329–42
Dröge F. 1977. *Astron. Astrophys.* 57:285–90
Duijveman A, Hoyng P, Machado ME. 1982. *Sol. Phys.* 81:137–57
Dulk GA. 1985. *Annu. Rev. Astron. Astrophys.* 23:169–224
Dulk GA. 1990. *Sol. Phys.* 130:139–50
Dulk GA, Bastian TS, Kane S. 1986. *Ap. J.* 300:438–47
Dulk GA, Dennis BR. 1982. *Ap. J.* 260:875–84
Dulk GA, Marsh KA. 1982. *Ap. J.* 259:350–58
Dumas G, Caroubalos C, Bougeret JL. 1982. *Sol. Phys.* 81:383–94
Fisher G. 1987. *Ap. J.* 317:502–13
Fleishman GD. 1994. *Sol. Phys.* 153:367–88
Fleishman GD, Kahler SW. 1992. *Ap. J.* 394:688–96
Fleishman GD, Yastrebov SG. 1994. *Sol. Phys.* 153:389–402
Fokker AD. 1965. *Bull. Astron. Inst. Neth.* 18: 111–24
Forrest DJ, Chupp EL. 1983. *Nature* 305:291–92
Fujiki K. 1997. *High spatial resolution imaging for the Nobeyama radioheliograph and observations of weak activities prior to solar flares,* PhD thesis. Univ. Tokyo, Japan

Fürst E, Benz AO, Hirth W. 1982. *Astron. Astrophys.* 107:178–85
Gary DE. 1985. *Ap. J.* 297:799804
Gary DE, Hartl M, Shimizu T. 1997. *Ap. J.* 477:958–73
Gary DE, Hurford GJ. 1990. *Ap. J.* 361:290–99
Gary DE, Hurford GJ. 1994. *Ap. J.* 420:903–12
Gopalswamy N, Kundu MR. 1995. In *Coronal Magnetic Energy Releases, Lect. Notes Phys*., ed. AO Benz, A Krüger, pp. 223–22. Berlin: Springer-Verlag
Gopalswamy N, Payne TEW, Schmahl EJ, Kundu MR, et al. 1994. *Astrophys. J.* 437: 522–28
Gopalswamy N, Raulin J-P, Kundu MR, Nitta N, Lemen JR, et al. 1995. *Ap. J.* 455:715–32
Gosling JT. 1993. *J. Geophys. Res.* 98:18937–49
Gosling JT, Hildner E, MacQueen RM, Munro RH, Poland AI, Ross CL. 1974. *J. Geophys. Res.* 79:4581–87
Gosling JT, McComas DJ, Phillips JL, Bame SJ. 1991. *J. Geophys. Res.* 96:7831
Güdel M, Aschwanden MJ, Benz AO. 1991. *Astron. Astrophys.* 251:285–97
Güdel M, Benz AO. 1990. *Astron. Astrophys.* 231:202–12
Güdel M, Wentzel D. 1993. *Ap. J.* 415:750–58
Güdel M, Zlobec P. 1991. *Astron. Astrophys.* 245:299–309
Guidice DA, Castelli JP. 1975. *Sol. Phys.* 44: 155–72
Haisch B, Strong KT, Rodono M. 1991. *Annu. Rev. Astron. Astrophys.* 29:275–324
Hamilton RJ, Petrosian V. 1992. *Ap. J.* 398:350–58
Hanaoka Y. 1996. *Sol. Phys.* 165:275–301
Hanaoka Y. 1997. *Sol. Phys.* 173:319–46
Holman GD. 1985. *Ap. J.* 293:584–94
Holman GD. 1995. *Ap. J.* 452:451–56
Holman GD, Eichler D, Kundu MR. 1980. In *Radio Physics of the Sun*, IAU Symp. 86, p. 457–61
Holman GD, Kundu MR, Kane S. 1989. *Ap. J.* 345:1050
Hoyng P, Duijveman A, Machado M, Rust DM, Svetska Z, et al. 1981. *Ap. J. Lett.* 244:L153–56
Hudson H. 1991. *Sol. Phys.* 133:357–69
Hudson H, Ryan J. 1995. *Annu. Rev. Astron. Astrophys.* 35:239–82
Hurford GJ, Read RB, Zirin H. 1984. *Sol. Phys.* 94:413–26
Isliker H. 1996. *Astron. Astrophys.* 310:672–80
Isliker H, Benz AO. 1994a. *Astron. Astrophys. Suppl.* 104:145–60
Isliker H, Benz AO. 1994b. *Astron. Astrophys.* 285:663–76
Kahler SW. 1977. *Ap. J.* 214:891–97
Kahler SW. 1992. *Annu. Rev. Astron. Astrophys.* 30:113–41
Kai K, Melrose DB, Suzuki S. 1985. See McClean & Labrum, 1985, pp. 415–41
Kane SR. 1981. *Ap. J.* 247:1113–21
Kane SR, Anderson KA. 1970. *Ap. J.* 162:1003–18
Kane SR, Crannell CJ, Datlowe D, Feldman U, Gabriel A, et al. 1980. In *Solar Flares*, ed. PA Sturrock, pp. 187–29. Boulder, CO: Assoc. Univ. Press
Karlicky M, Sobota M, Jiricka K. 1996. *Sol. Phys.* 168:375–83
Kaufmann P, Correia E, Costa JER, Zodi Vaz AM. 1986. *Astron. Astrophys.* 157:11–18
Kaufmann P, Costa JER, Dennis BR, Frost KJ, Orwig LE, et al. 1983. *Sol. Phys.* 84:311–19
Kerdraon A, Delouis J-M. 1997. In *Coronal Physics from Radio and Space Observations, Lect. Notes Phys*., ed. G Trottet, pp. 192–201. Berlin: Springer-Verlag
Khan JI. 1989. *Proc. Astron. Soc. Aust.* 8:29–31
Klein K-L. 1987. *Astron. Astrophys.* 183:341–50
Kocharov LG, Lee JW, Wang H, Zirin H, Kovaltsov GA, Usoskin IG, et al. 1994. *Sol. Phys.* 155:149–70
Komm R, Gary DE, Hurford GJ. 1998. *Ap. J.* In press
Korolkov DV, Pariiskii IUN. 1979. *Sky Telesc.* 57:324–39
Kosugi T. 1994. In *New Look at the Sun with Emphasis on Advanced Observations of Coronal Dynamics and Flares*, Nobeyama Radio Obs. Rep. 360, ed. S Enome, T Hirayama, pp. 11–18. Nobeyama, Japan: Nobeyama Radio Obs.
Kosugi T, Dennis BR, Kai K. 1988. *Ap. J.* 324:1118–36
Kosugi T, Makishima K, Murakami T, Sakao T, Dotani T, et al. 1991. *Sol. Phys.* 136:17–36
Kosugi T, Sakao T, Masuda S, Makishima K, Inda M, et al. 1992. *Publ. Astron. Soc. Jpn.* 44:45–49
Krucker S, Benz AO. 1994. *Astron. Astrophys.* 285:1038–46
Krucker S, Benz AO, Bastian TS, Acton LW. 1997a. *Ap. J.* 488:499–505
Krucker S, Benz AO, Delaboudiniere JP. 1997b. *Proc. Fifth SOHO Workshop, Oslo,* ESA Spec. Publ. 404, p. 465
Krüger A. 1979. *Introduction to Solar Radio Astronomy and Radio Physics.* Dordrecht: Reidel. 330 pp.
Krüger A, Voigt W. 1995. *Sol. Phys.* 161:393–405
Kucera TA, Dulk GA, Gary DE, Bastian TS. 1994. *Ap. J.* 433:875–85
Kuijpers J. 1974. *Sol. Phys.* 36:157–69
Kundu MR. 1961. *J. Geophys. Res.* 66:4308–12
Kundu MR, Bobrowsky M, Velusamy T. 1981. *Ap. J.* 251:342–51
Kundu MR, Gergeley TE, Szabo A, Loiacono

R, White SM. 1986. *Ap. J.* 308:436–42
Kundu MR, Nitta N, White SM, Shibasaki K, Enome S, et al. 1995a. *Ap. J.* 454:522–30
Kundu MR, Raulin JP, Nitta N, Hudson H, Shimojo M, et al. 1995b. *Ap. J.* 447:L135–37
Kundu MR, Raulin JP, Pick M, Strong KT. 1995c. *Ap. J.* 444:922–28
Kundu MR, Schmahl EJ, Velusamy T. 1982. *Ap. J.* 253:963–74
Kundu MR, Velusamy T, White SM. 1987. *Ap. J.* 321:593–605
Kundu MR, White SM, Gopalswamy N, Lim J. 1994. *Ap. J. Suppl.* 90:599–610
Lantos P, Pick M, Kundu MR. 1984. *Ap. J.* 283:71
Leblanc Y, Kuiper TBH, Hansen SF. 1974. *Sol. Phys.* 37:215–23
Lee JW, Gary DE. 1994. *Sol. Phys.* 153:347–65
Lee JW, Gary DE, Zirin H. 1994. *Sol. Phys.* 152:409–28
Lim J, Gary DE, Hurford GJ, Lemen JR. 1994. *Ap. J.* 430:425–34
Lim J, White SM, Kundu MR, Gary DE. 1992. *Sol. Phys.* 140:343–68
Lin RP. 1997. In *Coronal Physics from Radio and Space Observations*, ed. G Trottet, pp. 93–107. Berlin: Springer-Verlag
Lin RP, Levedahl WK, Lotko W, Gurnett DA, Scarf FL. 1986. *Ap. J.* 308:954–65
Lin RP, Schwarz RA, Kane SR, Pelling RM, Hurley KC. 1984. *Ap. J.* 283:421–25
Litvinenko, YuB. 1994. *Sol. Phys.* 151:195–98
Litvinenko, YuB. 1996. *Sol. Phys.* 167:321–31
Longcope D. 1996. *Sol. Phys.* 169:91–121
Lu E, Hamilton RJ. 1991. *Ap. J. Lett.* 380:L89–92
Lu E, Hamilton RJ, McTiernan JM, Bromund KR. 1993. *Ap. J.* 412:841–52
Lu E, Petrosian V. 1989. *Ap. J.* 338:1122–30
Lu E, Petrosian V. 1990. *Ap. J.* 354:735–44
Machado ME, Moore RL. 1986. *Adv. Space Res.* 6:217–26
Machado ME, Moore RL, Hernandez AM, Marta GR, Hagyard MJ, Smith JB. 1988. *Ap. J.* 326:425–50
Mandzhavidze N, Ramaty R. 1993. *Nucl. Phys. B Proc. Suppl.* 33A,B:141–60
Mangeney A, Pick M. 1989. *Astron. Astrophys.* 224:242–44
Marsh KA, Hurford GJ. 1982. *Annu. Rev. Astron. Astrophys.* 20:497–516
Marsh KA, Hurford GJ, Zirin H, Gulk GA, Dennis BR, et al. 1981. *Ap. J.* 251:797–804
Masuda S, Kosugi T, Hara H, Tsuneta S, Ogawara Y. 1994. *Nature* 371:495–97
McLean DJ, Labrum NR, eds. 1985. *Solar Radiophysics.* Cambridge, UK: Cambridge Univ. Press. 516 pp.
Melrose DB. 1980. *Plasma Astrophysics.* New York: Gordon & Breach. Vol. 2: 430 pp.
Melrose DB. 1990. *Aust. J. Phys.* 43:703–52
Melrose DB. 1995. *Ap. J.* 451:391–401
Melrose DB, Dulk GA. 1982. *Ap. J.* 259:844–58
Melrose DB, Dulk GA. 1984. *Ap. J.* 282:308–15
Melrose DB, Robinson PA, Feletto TM. 1995. *Sol. Phys.* 158:139–58
Mercier C, Trottet G. 1996. *Ap. J. Lett.* 474: L65–L68
Miller JA, Cargill PJ, Emslie AG, Holman GD, Dennis BR, et al. 1997. *J. Geophys. Res.* 102: 14631–59
Miller JA, LaRosa TN, Moore RL. 1996. *Ap. J.* 461:445–64
Miller JA, Ramaty R. 1987. *Sol. Phys.* 113:195–200
Nakajima H, Dennis BR, Hoyng P, Nelson G, Kosugi T, Kai K. 1985. *Ap. J.* 288:806–19
Nakajima H, Enome S, Shibasaki S, Nishio M, Takano T, et al. 1994. *Proc. Inst. Electr. Electron. Eng.* 82:705–13
Napier P, Thompson AR, Ekers RD. 1983. *Proc. Inst. Electr. Electron. Eng.* 71:1295–322
Nishio M, Yaji K, Kosugi T, Nakajima H, Sakurai T. 1997. *Ap. J.* 489:976–91
Nitta N, Kosugi T. 1986. *Sol. Phys.* 105:73–85
Pallavicini R, Serio S, Vaiana GS. 1977. *Ap. J.* 216:108–22
Parker EN. 1988. *Ap. J.* 330:474–79
Petrosian V. 1981. *Ap. J.* 251:727–38
Pick M, Ji SC. 1986. *Sol. Phys.* 107:159–65
Pick M, Raoult A, Trottet G, Vilmer N, Strong K, Magalhaes A. 1994. In *New Look at the Sun with Emphasis on Advanced Observations of Coronal Dynamics and Flares*, Nobeyama Radio Obs. Rep. 360, ed. S Enome, T Hirayama, pp. 263–66. Nobeyama, Japan: Nobeyama Radio Obs.
Pick M, van den Oord GHJ. 1990. *Sol. Phys.* 130:83–99
Pohjolainen S, Valtaoja E, Urpo S. 1996. *Astron. Astrophys.* 314:947–56
Poquerusse M, Steinberg JL, Caroubalos C, Dulk GA, MacQueen RM. 1988. *Astron. Astrophys.* 192:323–34
Preka-Papadema P, Alissandrakis CE. 1992. *Astron. Astrophys.* 257:307–14
Priest ER. 1991. *Philos. Trans. R. Soc. London Ser. A* 336:363–80
Priest ER, Forbes TG. 1986. *J. Geophys. Res.* 91:5579–88
Ramaty R. 1969. *Ap. J.* 158:753–70
Ramaty R, Mandzhavidze N, Kozlovsky B, Murphy RJ. 1995. *Ap. J. Lett.* 455:L193–96
Ramaty R, Murphy RJ. 1987. *Space Sci. Rev.* 45:213–68
Ramaty R, Petrosian V. 1972. *Ap. J.* 178:241–50
Ramaty R, Schwartz RA, Enome S, Nakajima H. 1994. *Ap. J.* 436:941–49
Ratcliff JA. 1959. *The Magnetoionic Theory*

and Its Application to the Ionosphere. Cambridge, UK: Cambridge Univ. Press. 206 pp.
Raulin JP, Kundu MR, Hudson HS, Nitta N, Raoult A. 1996. *Astron. Astrophys.* 306:299–312
Raulin JP, White SM, Kundu MR, Silva AVR, Shibasaki K. 1998. *Ap. J.* In press
Roberts JA. 1959. *Aust. J. Phys.* 12:327–55
Rosner R, Tucker WH, Vaiana GS. 1978. *Ap. J.* 220:643–65
Rosner R, Vaiana GS. 1978. *Ap. J.* 222:1104–8
Sakao T. 1994. *Characteristics of solar flare hard X-ray sources as revealed with the hard X-ray telescope aboard the Yohkoh satellite.* PhD thesis. Univ. Tokyo, Japan. 214 pp.
Sakao T, Kosugi T, Masuda S, Inda M, Makishima K, et al. 1992. *Publ. Astron. Soc. Jpn.* 44:L83–87
Sakao T, Kosugi T, Masuda S, Yaji K, Inda-Koide M, Makishima K. 1996. *Adv. Space Res.* 17:67–70
Sakurai T. 1982. *Sol. Phys.* 76:301–21
Sakurai T, Shibata K, Ichimoto K, Tsuneta S, Acton LW. 1992. *Publ. Astron. Soc. Jpn.* 44: 121–27
Sawant HS, Lattari CJB, Benz AO, Dennis BR. 1990. *Sol. Phys.* 130:57
Schmahl EJ, Kundu MR, Schmelz JT, Saba JLR, Stron KT. 1990. *Ap. J.* 358:654–64
Sharma RR, Vlahos L. 1984. *Ap. J.* 280:405–15
Sharma RR, Vlahos L, Papadopoulos K. 1982. *Astron. Astrophys.* 112:377–85
Shevgaonkar RK, Kundu MR. 1985. *Ap. J.* 292:733–51
Shibasaki K. 1996. *Adv. Space Res.* 17:135–37
Shibata K, Masuka S, Shimojo M, Hara H, Yokoyama T, et al. 1995. *Ap. J. Lett.* 451: L83–L85
Shimizu T. 1995. *Publ. Astron. Soc. Jpn.* 47: 251–63
Shimizu T, Tsuneta S, Acton LW, Lemen JR, Uchida Y. 1992. *Publ. Astron. Soc. Jpn.* 44:L147–53
Silva AVR, Gary DE, White SM, Lin RP, de Pater I. 1997. *Sol. Phys.* 175:157–73
Silva AVR, White SM, de Pater I, Shibasaki K, Hudson HS, Kundu MR. 1996. *Ap. J. Lett.* 458:L49–L52
Simnett GM. 1995. *Space Sci. Rev.* 73:387–432
Slottje C. 1978. *Nature* 275:520–21
Stähli M, Benz AO. 1987. *Astron. Astrophys.* 175:271–76
Stähli M, Gary DE, Hurford GJ. 1989. *Sol. Phys.* 120:351–68
Stähli M, Gary DE, Hurford GJ. 1990. *Sol. Phys.* 125:343–57
Starr R, Heindl WA, Crannell CJ, Thomas RJ, Batchelor DA, Magun A. 1988. *Ap. J.* 329:967–81
Steinacker J, Miller JA. 1992. *Ap. J.* 393:764–81
Steinberg J-L, Aubier-Giraud M, Leblanc Y, Boischot A. 1971. *Astron. Astrophys.* 10:362–76
Suzuki S, Dulk GA. 1985. See McLean & Labrum 1985, pp. 289–331
Swarup G. 1990. *Indian J. Radio Space Phys.* 19:493–505
Tajima T, Benz AO, Thaker M, Leboeuf JN. 1990. *Ap. J.* 353:666–77
Takakura T, Nishio M, Nakajima H, Enome S, Shibasaki K. 1994. *Publ. Astron. Soc. Jpn.* 46:653–63
Takano T, Nakajima H, Enome S, Shibasaki K, Nishio M, et al. 1997. In *Coronal Physics from Radio and Space Observations, Lect. Notes Phys*., ed. G Trottet, pp. 183–91. Berlin: Springer-Verlag
Tanaka K. 1987. *Publ. Astron. Soc. Jpn.* 39:1–45
Tapping KF, Kuijpers J, Kaastra KS, van Nieuwkoop J, Graham D, Slottje CL. 1983. *Astron. Astrophys.* 122:177–80
Tousey R. 1973. In *Space Research XIII*, ed. MJ Rycroft, SK Runcorne. Berlin: Akademie-Verlag. 713 pp.
Trulsen J, Fejer JA. 1970. *J. Plasma Phys.* 4: 825–41
Tsuneta S. 1985. *Ap. J. Lett.* 290:353–58
Tsuneta S, Acton L, Bruner M, Lemen J, Brown W, et al. 1991. *Sol. Phys.* 136:37–67
Velusamy T, Kundu MR. 1982. *Ap. J.* 258:388–92
Velusamy T, Kundu MR, Schmahl EJ, McCabe M. 1987. *Ap. J.* 319:984–92
Vilmer N, Trottet G. 1997. In *Coronal Physics from Radio and Space Observations*, ed. G Trottet, pp. 28–52. Berlin: Springer-Verlag
Vlahos L, Georgoulis M, Kluiving R, Paschos P. 1995. *Astron. Astrophys.* 299:897–911
Vlahos L, Machado ME, Ramaty R, Murphy RJ, Alissandrakis C, et al. 1986. In *Energetic Phenomena on the Sun*, ed. MR Kundu, B Woodgate, NASA Conf. Pub. 2439, 2:1–57
Wagner WJ, MacQueen RM. 1983. *Astron. Astrophys.* 120:136–38
Wang H, Gary DE, Lim J, Schwartz RA. 1994. *Ap. J.* 433:379–88
Wang H, Gary DE, Zirin H, Kosugi T, Schwartz RA, Linford G. 1995. *Ap. J. Lett.* 444:L115–18
Wang H, Gary DE, Zirin H, Nitta N, Schwartz RA, Kosugi T. 1996. *Ap. J.* 456:403–11
White SM, Kundu MR. 1992. *Sol. Phys.* 141:347–69
White SM, Kundu MR, Shimizu T, Shibasaki K, Enome S. 1995. *Ap. J.* 450:435–40

White SM, Kundu MR, Szabo A. 1987. *Sol. Phys.* 107:135–37
Wiehl HJ, Batchelor DA, Crannell CJ, Dennis BR, Price PN, Magun A. 1985. *Sol. Phys.* 96:339–56
Wild JP. 1950. *Aust. J. Sci. Res. A* 3:169–85
Wild JP, Smerd SF, Weiss AA. 1963. *Annu. Rev. Astron. Astrophys.* 1:291–366
Willes AJ, Robinson PA. 1996. *Ap. J.* 467:465–72
Willson RF. 1983. *Sol. Phys.* 83:285–303
Winglee RM, Dulk GA, Pritchett PL. 1988. *Ap. J.* 329:440–55
Yoshimori M. 1989. *Space Sci. Rev.* 51:85–115
Young CW, Spencer CL, Moreton GE, Roberts JA. 1961. *Ap. J.* 133:243–54
Zheleznyakov VV, Kocharovsky VV, Kocharovsky VLV. 1996. *Astron. Astrophys.* 308: 685–96
Zheleznyakov VV, Zlotnik EYa. 1963. *Sov. Astron.* 7:485–91